Batch settling curve registration via image data modeling

Nicolas Derlon[a,b], Christian Thürlimann[a,b], David Dürrenmatt[c], Kris Villez[a,1]

[a] *Eawag, Department Process Engineering, Überlandstrasse 133, CH-8600 Dübendorf, Switzerland*
[b] *Institute of Environmental Engineering, ETH Zürich, CH-8093 Zürich, Switzerland*
[c] *Rittmeyer AG, Inwilerriedstrasse 57, CH-6341 Baar, Switzerland*

Abstract

To this day, obtaining reliable characterization of sludge settling properties remains a challenging and time-consuming task. Without such assessments however, optimal design and operation of secondary settling tanks is challenging and conservative approaches will remain necessary. With this study, we show that automated sludge blanket height registration and zone settling velocity estimation is possible thanks to analysis of images taken during batch settling experiments. The experimental setup is particularly interesting for practical applications as it consists of off-the-shelf components only, no moving parts are required, and the software is released publicly. Furthermore, the proposed multivariate shape constrained spline model for image analysis appears to be a promising method for reliable sludge blanket height profile registration.

Keywords: secondary clarifiers, separation processes, shape constrained splines, sludge blanket height, sludge settling, wastewater treatment

List of acronyms

Acronyms	Full expression
AO	Automated, on-line
QR	Qualitative representation
SBH	Sludge blanket height
SCS	Shape constrained splines
VO	Visual, off-line
VS, VS1, VS2	Visual, simultaneous
ZSV	Zone settling velocity

List of Symbols.

Symbol	Definition
$\boldsymbol{\beta}$	All spline function coefficients
$\boldsymbol{\beta}_k$	Coefficients of the kth spline function
$\boldsymbol{\theta}$, θ_t	Transitions (tth transition)
Θ	Feasible set for $\boldsymbol{\theta}$
Ω	Feasible set for $\boldsymbol{\beta}$
$\underline{\boldsymbol{b}}$, $\overline{\boldsymbol{b}}$, $\underline{b_e}$, $\overline{b_e}$	Interval boundaries (for episode e)
d	Derivative index
e	Episode index
f_k	kth function
$f_k^{(d)}$	dth derivative of the kth function
g	Objective function
j	Pixel index
$\hat{h}$, $\hat{\boldsymbol{h}}_{AO}$, $\hat{\boldsymbol{h}}_{VO}$, $\hat{\boldsymbol{h}}_{VS1}$, $\hat{\boldsymbol{h}}_{VS2}$	Sludge blanket height (SBH) estimates (AO/VO/VS1/VS2: see list of acronyms)
h_L, h_U	Physical height corresponding to the top/bottom (U/L) pixel
i	Image index
k	Data series index, color channel index
r_v	Parameter of the Vesilind equation
q	Flux
$s_{e,d+1}$	Sign for the dth derivative in the eth episode
u	Integration variable
v	Settling velocity

v_0	Parameter of the Vesilind equation
x, x_h	Pixel position (for the hth row in $\tilde{\boldsymbol{Y}}$)
$\boldsymbol{x}$	Independent data vector, pixel positions
z, $\boldsymbol{z}_{AO}$, $\boldsymbol{z}_{VO}$, $\boldsymbol{z}_{VS}$	Sludge blanket height (SBH) sampling times (AO/VO/VS1/VS2: see list of acronyms)
$\boldsymbol{B}_k$	Basis matrix for f_k
D_k	Maximum considered derivative degree for the shape constraints applied to f_k
E	Number of episodes
I	Number of images in an experiment
J	Number of functions to fit
H	Number of rows in $\tilde{\boldsymbol{Y}}$
K	Number of data series to approximate, number of color channels
$\boldsymbol{S}$	Matrix describing the qualitative sequence, i.e. series of primitives
T	Number of transitions
$\boldsymbol{Y}$	Model estimates
$\tilde{\boldsymbol{Y}}$	Measurement matrix

1. Introduction

Settling is one of the key processes in activated sludge wastewater treatment plants (WWTPs, Ekama et al., 1997). Its primary function is the clarification of mixed liquor, thereby preventing wasting organic material and nutrients into the water bodies that receive the treated wastewater. In addition, settling results in the thickening of sludge thereby increasing the efficiency of biological conversion processes occurring in the reactor tanks of the WWTPs. Accurate design of settlers requires a proper characterization of the sludge settling properties. In addition, WWTP operation can be improved by avoiding overloaded settler conditions or increasing the reactor efficiency by *(i)* manipulation of the recycle flow rate (Balslev et al., 1994; Chen and Beck, 2001; Mines Jr et al., 2001), *(ii)* step feed (also: step aeration) and step sludge control (Chen and Beck, 2001), or *(iii)* short-term use of the reactor tanks for sludge sedimentation and storage. Settling also plays an essential role during the primary clarification process. Inefficient removal of suspended solids prior to biological treatment results in higher oxygen demand (for oxidizing organic pollution) and lower biogas production. For innovative technologies, such as granular sludge processes, settling governs the separation of the slow and fast settling biomass, i.e., the selection of the granules and the selective removal of flocs through excess sludge removal. A proper characterization of the settling properties of the sludge is thus necessary for a variety of separation processes that can be found on small and large WWTPs.

Different parameters are available to characterize the sludge settling properties (van Loosdrecht et al., 2016): the sludge volume index (SVI), the diluted sludge volume index (DSVI), the stirred specific volume index at 3.5 min (SSVI3.5), etc. Unfortunately, such measures provide an incomplete description of the sludge settling properties (van Loosdrecht et al., 2016). A more detailed characterization of the sludge settleability is provided by sludge blanket height (SBH) profiles (van Loosdrecht et al., 2016). However, measuring such profiles is significantly more time-consuming than measuring sludge settling properties (SVI, etc.). Therefore, several empirical correlations were proposed to link the settling model parameters to the sludge settling measures that are easy to obtain. Such empirical correlations form the basis of today's practice, including control systems (e.g., Traoré et al., 2006). and despite known limits reported in several studies (Ozinsky and Ekama, 1995a,b; Bye and Dold, 1998).

A dynamic settling model commonly used in today's practice is the exponential model first proposed in Vesilind (1968). Still, several more detailed models have been built and studied (e.g., Cacossa and Vaccari, 1994; Plósz et al., 2007; Ramin et al., 2014; Li and Stenstrom, 2016). Critical to any study of settling behavior is the collection of SBH profiles registered during batch settling experiments as discussed above. All of the aforementioned studies rely on SBH measurements obtained by visual inspection of a settling column during the batch settling experiments. Typical use of SBH profiles may provide only one data point per experiment, e.g. when the zone settling velocity (ZSV) measurement corresponding to a single total suspended solids concentration is of interest only. As a result, collecting sufficient data to empirically describe the zone settling velocity and flux curves is a cumbersome and time-intensive task that can be afforded within research projects but is rarely executed routinely on WWTPs, as already reported in Daigger and Roper Jr (1985). The potential of the developed settling models for optimization or control of WWTP operation is likely only realized if a routinely applicable yet inexpensive method for SBH registration is available. The lack of an easy, quick, and reliable method for the measurement of batch settling curves is still one of the main limitations for both research and practice (Li and Stenstrom, 2014). We therefore focus on the problem of batch settling curve registration yet also demonstrate how the resulting batch settling profiles can be used for dynamic modeling.

Devices for automated SBH registration are available today (e.g., Vanrolleghem et al., 2006). However, they are likely too expensive to obtain and maintain for routine monitoring purposes. Methods to automate and/or advance SBH registration include *(i)* light intensity scanning (Vanrolleghem et al., 1996), *(ii)* measurement of a radioactive tracer (De Clercq et al., 2005), *(iii)* use of an ultrasonic transducer (Locatelli et al., 2015), and (iv) high-speed camera imaging (Mancell-Egala et al., 2016). The applicability of such techniques may remain limited unless *(i)* on-site use is feasible to avoid effects of sample deterioration and *(ii)* the devices are easy to maintain by technical staff on typical wastewater treatment plants.

The main objective of our work is to produce, demonstrate, and validate a novel method for automated image-based SBH registration. Automated sample preparation is considered for future study. The proposed method for batch settling curve registration consists of *(i)* using an inexpensive off-the-shelf camera to collect images during multiple batch settling experiments and *(ii)* fitting a shape constrained spline (SCS) model extended for the purpose of image analysis. The main advantage of our method is that the experimental method is accessible to researchers and practitioners as only inexpensive off-the-shelf equipment is used. A side benefit of applying the SCS model is that it enables use of multi-channel data present in the collected images and avoids differentiation of the noisy data during image analysis, in contrast to existing methods (e.g., Kim et al., 2011).

The proposed method exploits knowledge about the expected shape of the light intensity profile along the vertical dimension of the sludge column. Using shape information to characterize settling behavior is not new however. For example, it is known that the SBH profile obtained with conventional batch settling experiments with ideal suspensions is described as a convex profile, corresponding to a convex section of the solids flux curve that governs such experiments. Similarly, recently proposed batch experiments deliver concave height profiles governed by concave sections of the solids flux curve. Knowledge about the shape is exploited in Diehl (2007); Bürger and Diehl (2013); Diehl (2015). Our work is different from these historical approaches in two ways. First, our method allows fitting functions which have a changing shape along their domain, as opposed to previous work. In our particular study, functions consisting of a concave segment followed by a convex segment are estimated. Secondly, the convex-concave shape enables explicit accounting of non-ideal behavior during experiments. Indeed, we study batch settling experiments where the effects of turbulence at the start of the experiments cannot be ignored. In what follows, the most important aspects of our method and the most significant results are explained.

2. Materials and Methods

2.1. Batch Settling Experiments

Nine batch settling experiments have been executed. Each of the settling experiments is executed for a dilution of a granular sludge sample obtained from a column sequencing batch reactor located at Eawag and fed with low-strength municipal wastewater. Two such samples were taken directly from the reactor as source material for diluted sludge sample preparation. The sludge sample index and the applied dilutions for each of the experiments are given in Table 1. The total suspended solids concentration on the day of experimentation was 2.4 g/L. Throughout experimentation, a 2 L vertical glass cylinder is used. Each batch settling experiment was started by filling the glass cylinder with the (diluted) sludge and by ensuring homogeneity at the start of the experiment by means of manual stirring with a glass rod.

A scheme of the experimental set up can be seen in Fig. 1. During each experiment, images are taken by means of a digital camera (Camera 1, Canon PowerShot G9) equipped with a continuous power supply and modified with the Canon Hack Development Kit (CHDK, 2016) software to continuously capture images at intervals of 15s. Camera 1 was positioned so that *(i)* the height of the camera corresponds to the top of the sludge column, *(ii)* the central line of sight of the camera is directed at the top of the sludge column and *(iii)* the complete column is visible in the image. Within each experiment, the images are indexed with i ($i = 1, \ldots, I$).

In experiments 5 and 6, two experimenters (experimenter 1 and 2) registered the SBH by means of visual inspection of the settling sludge column at time intervals of 30s as conventional experimentation (van Loosdrecht et al.,

2016) and as close as possible to every 2nd image registration by camera 1. Results obtained by the experimenters are indicated with the subscripts $_{\mathrm{VS1}}$ and $_{\mathrm{VS2}}$ (visual, simultaneous). In addition, a second camera (Camera 2; Samsung Galaxy S5, Model No.: SM-G800F, OS: Android 4.4.2) was used to collect simultaneous close-up images of the sludge blanket at time intervals of 30s by means of frame lapse recording software (Framelapse by Neximo Labs, v2.1.1). Camera 2 was moved manually during each batch experiment by a third experimenter so to match the visually recognized SBH as close as possible. Results obtained with the close-up images are referred to by the subscript $_{\mathrm{VO}}$ (visual, off-line).

2.2. Shape Constrained Spline Function Fitting

The proposed image-based sludge blanket registration method consists of an extension of the pre-existing SCS method reported in Villez et al. (2013). Whereas the original method only allows analysis of univariate signals, the extended method permits simultaneous fitting of multiple SCS functions to multivariate data series. Each of fitted functions is however subject to the same shape constraints. Each part of the method SCS method is introduced generally followed by a discussion of details pertaining to the analysis of image data.

2.2.1. Modeled Data

General treatment. The measurements are given as a $J \times K$ matrix $\tilde{\boldsymbol{Y}}$ of which $y_{j,k}$ is the element in the jth row and kth column and $\tilde{\boldsymbol{Y}}_{\cdot,k}$ is the kth column vector. Each row vector $\tilde{\boldsymbol{Y}}_{j,\cdot}$ is associated with the jth element of $\boldsymbol{x}$ which is the $J \times 1$ vector containing the values of a single independent variable.

Application. The analyzed data sets correspond to rectangular selections of red-blue-green images (see the *Supplementary Information,* Fig. S.1). A rectangular section of the image is selected so that the horizontal dimension of the selection covers the center of the photographed column and has the 200 mL and 1000 mL marks on the column as limits in the vertical dimension. The width of the section is arbitrarily set to 51 pixels for all experiments. The heights of the image sections changed slightly across experiments and are reported in Table 1. All color channels (3) are included for analysis.

The data in each image are initially organized as a 3-D array with dimensions corresponding to the vertical image dimension, the horizontal image dimension, and the color channel. For the purpose of analysis, we consider each set of 51 light intensities corresponding to the same vertical position and color channel as repeated measurements of the same light intensity. To generate a 2-D matrix of the form $\tilde{\boldsymbol{Y}}$ the following *unfolding* procedure is executed. One first retrieves the matrix of light intensity values in the top row of pixels in the image and defines this matrix as $\tilde{\boldsymbol{Y}}$. This matrix has dimensions 51×3. One continues by selecting the same matrix for the second row and places this matrix below the previously obtained matrix. This concatenation process is continued until the bottom row pixels are reached and added. At this stage, the matrix $\tilde{\boldsymbol{Y}}$ is completed. The corresponding vector $\boldsymbol{x}$ contains the row pixel index for each row in $\tilde{\boldsymbol{Y}}$. In the case of experiment 6, the dimensions of the matrix $\tilde{\boldsymbol{Y}}$ are $J = 1287 \times 51 = 65637$ and $K = 3$. The independent data vector ($\boldsymbol{x}$) contains the corresponding pixel positions, meaning that each of the 1287 vertical pixel positions appears 51 times within $\boldsymbol{x}$.

2.2.2. Data Model and Definition of Optimality

General treatment. The multivariate data series are modeled by means of K spline functions, $f_k(\boldsymbol{\beta}, \boldsymbol{x})$ $(k = 1, \ldots, K)$ (Ramsay and Silverman, 2005). The choice for spline functions is especially motivated by the fact that shape constraints applied to non-empty intervals of a spline function domain can be formulated as a finite number of equality and inequality constraints (see e.g., Papp and Alizadeh, 2014; Villez et al., 2013; Villez and Habermacher, 2016). The degrees of the spline functions are given as D_k. Internal spline knots determine where one polynomial segment ends and the next one starts. They can be placed in arbitrary locations within $[x_1, x_J]$. Because of our function choice, each function is linear in the spline coefficients (function parameters). More specifically, the spline function model generates estimates of the measured variables ($\boldsymbol{Y}$) given function parameters ($\boldsymbol{\beta}$) as follows:

$$\boldsymbol{Y}(\boldsymbol{\beta}) = \boldsymbol{f}(\boldsymbol{\beta}, \boldsymbol{x}) \tag{1}$$

with:

$$\begin{aligned} \boldsymbol{f}(\boldsymbol{\beta}, \boldsymbol{x}) &= \left[\begin{array}{ccccc} f_1(\boldsymbol{\beta}_1, \boldsymbol{x}) & \ldots & f_k(\boldsymbol{\beta}_k, \boldsymbol{x}) & \ldots & f_K(\boldsymbol{\beta}_K, \boldsymbol{x}) \end{array} \right] \\ &= \left[\begin{array}{ccccc} \boldsymbol{B}_1(\boldsymbol{x})\, \boldsymbol{\beta}_1 & \ldots & \boldsymbol{B}_k(\boldsymbol{x})\, \boldsymbol{\beta}_k & \ldots & \boldsymbol{B}_K(\boldsymbol{x})\, \boldsymbol{\beta}_K \end{array} \right] \end{aligned} \tag{2}$$

$$\boldsymbol{\beta} = \left[\begin{array}{cccccc} {\boldsymbol{\beta}_1}^{\mathrm{T}} & {\boldsymbol{\beta}_2}^{\mathrm{T}} & \cdots & {\boldsymbol{\beta}_k}^{\mathrm{T}} & \cdots & {\boldsymbol{\beta}_K}^{\mathrm{T}} \end{array} \right]^{\mathrm{T}} \tag{3}$$

In the above, the matrices $\boldsymbol{B}_k(\boldsymbol{x})$ correspond to the evaluation of the spline basis of the kth function in the arguments $\boldsymbol{x}$.

The model is fitted to the data by minimizing the following least-squares lack-of-fit:

$$g(\boldsymbol{\beta}) = \sum_{j=1}^{J}\sum_{k=1}^{K}\left(\tilde{\boldsymbol{Y}}_{j,k} - \boldsymbol{Y}_{j,k}(\boldsymbol{\beta})\right)^2 \tag{4}$$

For primers on spline models, we refer to Hastie et al. (2001) and Ramsay and Silverman (2005).

Application. In the present study, three natural cubic ($K = 3$) B-spline functions are fitted to three column vectors of $\boldsymbol{Y}$. Internal spline knots are placed at every 8th pixel following the first pixel for all functions (i.e., x_9, $x_{17}, \ldots$). This knot placement was found to deliver sufficient flexibility to the fitted functions while ensuring a reasonably short computational effort. As both the knot locations and independent data vectors are the same for each function, the matrices $\boldsymbol{B}_k(\boldsymbol{x})$ are the same for every function (i.e., $\boldsymbol{B} = \boldsymbol{B}(\boldsymbol{x}) = \boldsymbol{B}_k(\boldsymbol{x}), k = 1, \ldots, K$).

2.2.3. Shape Constraints

General treatment. During model fitting, the spline functions are constrained to have a predefined shape. The assumed shape can be derived from expert knowledge or based on rigorous qualitative simulation (Kuipers, 1994; Shaich et al., 2001; Bredeweg et al., 2009). In either case, the shape is defined as a sequence of E *episodes* ($e = 1, \ldots, E$). These episodes are contiguous intervals of the function domain within which a number of the function's derivatives do not change sign. Such a sequence is known as a *qualitative sequence*. It is defined mathematically as a matrix $\boldsymbol{S}$ with $\boldsymbol{S}(e, d+1) = s_{e,d+1}$ specifying the sign of the dth derivative in the eth episode. The elements of $\boldsymbol{S}$

can taken on the integer values +1, 0, and −1 to indicate positive, zero, and negative signs of the derivatives. When the sign is unspecified, a question mark (?) is used instead. The matrix $\boldsymbol{S}$ is specified a priori. The episodes themselves are defined by $T = E - 1$ transitions, $\boldsymbol{\theta}$ ($\theta_t = \boldsymbol{\theta}(t)$; $t = 1, \ldots, T$), which are the function argument values where the episodes meet and which need to be estimated. The complete description of the shape of a function by means of $\boldsymbol{S}$ and $\boldsymbol{\theta}$ is known as a *qualitative representation* (QR).

Application. The fitted functions are constrained to have a shape defined by two episodes. The first episode has a concave shape, i.e. a negative sign for the second derivative. The second episode has a convex shape and decreasing. Consequentially, one writes $\boldsymbol{S}$ as a matrix with two rows, one for each episode:

$$\boldsymbol{S} = \begin{bmatrix} ? & ? & -1 & ? \\ ? & -1 & +1 & ? \end{bmatrix}. \tag{5}$$

The corresponding QR thus exhibits a single transition which corresponds to the location of the inflection point between the two episodes: $\boldsymbol{\theta} = \theta = \theta_1$.

2.2.4. Optimization

General treatment. With the above definitions, the least-squares SCS function fitting problem is written mathematically as follows:

$$\hat{\boldsymbol{\beta}}, \hat{\boldsymbol{\theta}} = \arg\min_{\boldsymbol{\beta}, \boldsymbol{\theta}} g(\boldsymbol{\beta}, \boldsymbol{\theta}) = \sum_{j=1}^{J} \sum_{k=1}^{K} \left(|\boldsymbol{Y}_{j,k} - \boldsymbol{Y}(\boldsymbol{\beta})_{j,k}|^2 \right) \tag{6}$$

$$\text{s.t.} \quad \boldsymbol{\beta} \in \Omega(\boldsymbol{\theta}, \boldsymbol{S}) \tag{7}$$

$$\boldsymbol{\theta} \in \Theta \tag{8}$$

and subject to the linear constraints Eq. 1–3. In the above, Θ is the set containing all feasible values for $\boldsymbol{\theta}$ and $\Omega(\boldsymbol{\theta}, \boldsymbol{S})$ is the set containing all values for $\boldsymbol{\beta}$ satisfying the shape constraints. Θ is defined mathematically as follows:

$$
\begin{aligned}
&\boldsymbol{\beta} \in \Omega(\boldsymbol{\theta}, \boldsymbol{S}) \\
&\quad\Updownarrow \\
&\forall d = 0, \ldots, D_k, \forall k = 1, \ldots, K, \forall x \in [x_1, x_J] : \\
&\qquad f_k^{(d)}(\boldsymbol{\beta}_k, x) \begin{cases} \geq 0, & \text{if } \underline{b_e} \leq x \leq \overline{b_e} \wedge \boldsymbol{S}(e, d+1) = +1 \\ = 0, & \text{if } \underline{b_e} \leq x \leq \overline{b_e} \wedge \boldsymbol{S}(e, d+1) = 0 \\ \leq 0, & \text{if } \underline{b_e} \leq x \leq \overline{b_e} \wedge \boldsymbol{S}(e, d+1) = -1 \end{cases} \\
&\qquad \underline{\boldsymbol{b}} = \begin{bmatrix} \underline{b_1} & \underline{b_2} & \ldots & \underline{b_e} & \ldots & \underline{b_{E-1}} & \underline{b_E} \end{bmatrix} \\
&\qquad\quad = \begin{bmatrix} x_1 & \theta_1 & \ldots & \theta_{t-1} & \ldots & \theta_{T-1} & \theta_T \end{bmatrix} \\
&\qquad \overline{\boldsymbol{b}} = \begin{bmatrix} \overline{b_1} & \overline{b_2} & \ldots & \overline{b_e} & \ldots & \overline{b_{E-1}} & \overline{b_E} \end{bmatrix} \\
&\qquad\quad = \begin{bmatrix} \theta_1 & \theta_2 & \ldots & \theta_t & \ldots & \theta_T & x_J \end{bmatrix}.
\end{aligned}
\tag{9}
$$

with $f_k^{(d)}(\cdot, u)$ the dth derivative of $f_k(\cdot, u)$ with respect to u.

The objective function (Eq. 7) is quadratic in $\boldsymbol{\beta}$. The shape constraints (Eq. 9) are convex in $\boldsymbol{\beta}$. In the case of univariate spline functions, as in this study, they can be formulated as a finite number of necessary and sufficient inequality constraints (Papp and Alizadeh, 2014). As a result, the problem has a single optimum and can be solved efficiently to global optimality given values for $\boldsymbol{\theta}$. Consequentially, the complete optimization problem can be solved as a nested optimization problem where the values for $\boldsymbol{\beta}$ are repeatedly obtained for considered candidate values for $\boldsymbol{\theta}$. The above problem is however non-convex and possibly multi-modal in $\boldsymbol{\theta}$. Still, globally optimal estimates for $\boldsymbol{\theta}$ can be found by means of the branch-and-bound algorithm as used in Villez et al. (2013); Villez and Habermacher (2016). The bounding procedures and their proofs are similar to those presented in Villez et al. (2013); Villez and Habermacher (2016) and are given in the *Supplementary Information*. Importantly, the bounding gap does not converge to zero in the multivariate case, in contrast to results obtained for the univariate case ($K = 1$) studied in Villez et al. (2013). This situation is however similar to the case studied in Villez and Habermacher (2016), where the presence of discontinuous trends in univariate data series was explicitly accounted for. For more details we refer to the *Supplementary Information*.

Application. The feasible set for the transition is the function domain, i.e. $\Theta := [x_1, x_J]$. Optimization of $\boldsymbol{\theta}$ is continued until a tolerance of 1/8 of a pixel is achieved for the optimal position of the inflection point. This optimization is repeated for each image registered with camera 1 in each of the experiments. For a given experiment, the obtained value ($\hat{\theta}$) for image i is given as $\hat{\theta}_{\mathrm{SCS},i}$.

2.3. Sludge Blanket Height Registration Methods

SBH estimates are obtained with four distinct methods. The first two methods are automated. A third method is based on off-line visual inspection of the close-up images of the sludge blanket. The fourth method consists of registering the SBH visually during the batch experiments by two experienced experimenters. More details follow next.

2.3.1. Automated Sludge Blanket Height Registration with the Shape Constrained Splines Method

Following optimization as described above, the location of the inflection points (θ) are given as a vertical pixel position (direction: top-down) within the analyzed segment of the images. To obtain the SBH for image i in a given experiment, measured from the bottom of the glass column, the following linear expression is used:

$$\hat{h}_{\mathrm{SCS},i} = h_L + (h_U - h_L) \cdot \left(1 - \frac{\hat{\theta}_{\mathrm{SCS},i} - x_J}{x_1 - x_H}\right), \quad i = 1, \ldots, I \qquad (10)$$

with previously undefined parameters given in Table 1. The complete time series of SBH estimates is given as the vector $\hat{\boldsymbol{h}}_{\mathrm{SCS}}$ and the corresponding sampling time vector as $\boldsymbol{z}_{\mathrm{SCS}}$.

2.3.2. Automated Sludge Blanket Height Registration with the Maximum Slope Method

In Kim et al. (2011) an image analysis method for sludge blanket registration is proposed and positively evaluated. For every pixel along the vertical column dimension, one computes a slope parameter, S_j, as the difference between the light intensity at the considered pixel and the light intensity at the lowest pixel divided by the absolute distance between the considered pixel and the lowest pixel:

$$S_j = \frac{y_j - y_J}{|x_j - x_J|} \qquad (11)$$

with y_j and y_J light intensities for a single color channel obtained within a single column of pixels. The pixel j corresponding to a maximal slope is referred to as the knee in the light intensity profile and is identified as the sludge blanket height. Note that the definition of such a knee is different from the definition of an inflection point. In Kim et al. (2011) this is executed with only one column of pixels in the recorded images and with the red color channel only. Following pixel location, the sludge blanket height is computed by linear interpolation as above ((10)). The maximum slope (MS) method is implemented as in Kim et al. (2011) except for the following modifications:

1. Instead of selecting one column of pixels, the light intensity data are averaged along the horizontal dimension prior to analysis. The pixel selection is the same as for the shape constrained spline method.
2. Instead of computing the slope for every pixel, the slope is only computed for the first 1250 pixels. This avoids errors due to noise as will be demonstrated below.

The sludge blanket heights obtained with the MS method are reported as $\hat{\boldsymbol{h}}_{\mathrm{MS}}$ and the corresponding time instants as $\boldsymbol{z}_{\mathrm{MS}}$.

2.3.3. Visual Sludge Blanket Height Registration via Close-up Inspection after Experimentation

The third method to establish SBH estimates is based on a visual inspection of close-up images after the experiment is finished. The close-up images are used as a reference in what follows. The obtained SBHs are given as the vector $\hat{\boldsymbol{h}}_{\mathrm{VO}}$. The corresponding time instants are given as $\boldsymbol{z}_{\mathrm{VO}}$.

2.3.4. Conventional Sludge Blanket Height Registration during Experimentation

A 4th and 5th SBH estimate is obtained by means of a visual inspection of the glass column during the batch experiment. These SBH estimates are referred to as $\hat{\boldsymbol{h}}_{\mathrm{VS1}}$ and $\hat{\boldsymbol{h}}_{\mathrm{VS2}}$. The times of registration are the same for both estimates and are given as $\boldsymbol{z}_{\mathrm{VS}}$.

2.4. Zone Settling Velocity Estimation

Each of the obtained SBH profiles can be used to model hindered and compressed settling in detail as described in Torfs et al. (2016) and as also discussed in the introduction. Given our focus on SBH registration, we demonstrate the utility of the method by computing the ZSV, which reflects on the hindered settling only and is conceptually simpler compared to compressed settling model identification procedures. The ZSV is computed by means of locating the inflection point with negative tangent slope in the considered SBH profile (e.g., Vanderhasselt and Vanrolleghem, 2000). Indeed, the shape of the profile is known to consist of a downward concave episode followed by a downward convex episode with the transition corresponding to the SBH. The sign matrix $\boldsymbol{S}$ thus is:

$$\boldsymbol{S} = \begin{bmatrix} ? & - & - & ? \\ ? & - & + & ? \end{bmatrix} \tag{12}$$

To obtain the ZSV from the SBH estimates obtained via SCS-based image analysis, the optimization problem described above (Eq. 7–9) is modified as follows. The data model is changed so that the univariate vector containing the SBH profile are approximated with a single univariate cubic spline function with knots at every sampling time:

$$K = 1 \tag{13}$$

$$\tilde{\boldsymbol{Y}} = \tilde{\boldsymbol{Y}}_{\cdot,1} = \tilde{\boldsymbol{y}}_k = \hat{\boldsymbol{h}}_{\mathrm{SCS}} \tag{14}$$

$$\boldsymbol{x} = \boldsymbol{z}_{\mathrm{SCS}} \tag{15}$$

All other settings are kept the same so that a least-squares fit of a SCS function to the SBH profile is obtained. Importantly, the modified optimization problem reduces to the univariate case studied in Villez et al. (2013). As a result, the best location of the inflection point can be determined with absolute precision and global optimality. Upon fitting the SCS function, the ZSV is obtained by computing the first derivative (tangent slope) in the inflection point. The absolute tangent slope is reported as the ZSV. This is executed for every experiment.

The above computation of the ZSV is also executed for the SBH estimates obtained with off-line and simultaneous visual inspection by replacing the dependent data vector $\tilde{\boldsymbol{y}}_k$ with the data series containing the SBH estimates ($\hat{\boldsymbol{h}}_{\mathrm{VO}}$, $\hat{\boldsymbol{h}}_{\mathrm{VS1}}$, $\hat{\boldsymbol{h}}_{\mathrm{VS2}}$, $\hat{\boldsymbol{h}}_{\mathrm{MS}}$) and the independent data vector with the corresponding image and SBH registration times. The ZSVs are obtained for experiments 5 and 6.

2.5. Data and Software

All data and software required to reproduce the results of this study are released publicly with a GPL v3 license and are added to the *Supplementary Information*.

3. Results

3.1. Demonstration of the Shape Constrained Splines Method for Automated Sludge Blanket Height Registration

Fig. S.1 shows a section of a single image obtained during experiment 5. The pixels selected for further analysis are indicated with yellow lines. Fig. 2 shows the corresponding light intensity measurement as a function of the pixel index for the three channels. While the data series exhibit considerable levels of noise, one clearly observes the sludge blanket as an inflection point in the data series. The inflection point corresponds to the discontinuity in the sludge concentration better known as the SBH. Solving the SBH estimation problem (Eq. 7–9) delivers three optimized SCS functions -one for each color channel- with the same concave-convex shape and the same location for the inflection point. The SCS functions and the pixel index corresponding to the identified sludge blanket (1056) are also shown in Fig. 2.

3.2. Demonstration of the Maximum Slope Method for Automated Sludge Blanket Height Registration

In the top panel of Fig. 3 one can see the average light intensity for the red color channel as a function of the pixel index for image considered above. The slope values are given in the bottom panel. One can see that selecting the pixel with the MS method results in the selection of the second last pixel at the bottom the image. This is caused by substantial noise amplification of the slope computation especially close to the reference pixel at the bottom of the image. The modified method considering the top 1225 pixels selects pixel 977, which is a more sensible choice. However, a human observer may instead select pixel 1035 as the knee. This difference is again explained by noise amplification of the slope computation. However, even pixel 1035 is higher in the image compared to the shape constrained spline method result (1056). This is explained by the fact that the maximal slope method selects a location for a knee point rather than an inflection point.

3.3. Sludge Blanket Height Profiles

Fig. 4 shows a composite image obtained by collating the analyzed segments of the images taken from the 127 consecutive images collected during experiment 5. The image is presented here without any modification, mainly to visualize the rather low contrast in the collected images. The pixel heights corresponding to the SCS-based inflection points ($\hat{\boldsymbol{\theta}}_{\mathrm{SCS}}$) and the MS knee ($\hat{\boldsymbol{\theta}}_{\mathrm{MS}}$) are also indicated in the collated image. Close inspection reveals that the SCS-based inflection points correspond to the SBH at the front of the cylindrical column. One can see a semi-dark area above the identified inflection points. The top of the semi-dark area correspond to the back of the cylindrical column. The fact that the front and back side of the sludge blanket can be distinguished is a consequence of the applied position and angle of the camera. The MS knee pixel cannot be tied easily to any of the two sludge blanket features in the images. In addition, the MS knee profile appears to be more erratic than the profile of the inflection points. The collated images with and without SBH estimates obtained for all experiments are available in the *Supplementary Information*.

In experiments 5 and 6, all considered methods for SBH registration were applied. In Fig. 5 one can see the obtained SBH estimates. The SBH estimates obtained with close-up visual inspection and by simultaneous visual inspection ($\hat{\boldsymbol{h}}_{\mathrm{VO}}$, $\hat{\boldsymbol{h}}_{\mathrm{VS1}}$, and $\hat{\boldsymbol{h}}_{\mathrm{VS2}}$) appear fairly close to each other. The SCS-based SBH estimates ($\hat{\boldsymbol{h}}_{\mathrm{SCS}}$) are about 70 mL higher in the concave episode (hindered and compressed settling) for experiment 5 and about 30 mL lower for experiment 6. For the MS method, the offset is $+100$ mL for experiment 5 and -5 mL for experiment 6.

Each of the obtained SBH profiles shown in Fig. 4 and Fig. 5 can be described as a decreasing trend that is composed of a concave episode followed by a convex episode. As in previous studies (e.g., Diehl, 2015), the concave episode is explained as a result from turbulence stemming from the stirring and possibly flocculation before the start of the experiment. Such behavior is generally considered non-ideal as the first data points do not provide information about the settling process. To account for this, one can model the effect of turbulence explicitly (e.g., Diehl, 2015) or manipulate the data to remove the concave episode entirely (e.g., De Clercq, 2006). In this work, we fit a shape constrained spline function to the SBH profiles with the desired concave-convex shape. The resulting functions for experiments 5 and 6 are shown in Fig. 5. The standard error for each SBH measurement profiles, obtained by taking the fitted curve with the close-up SBH profile ($\hat{\boldsymbol{h}}_{\mathrm{VO}}$) as a reference, are reported in Table 2. The reference curve fits the close-up SBH profile best, as expected since $\hat{\boldsymbol{h}}_{\mathrm{VO}}$ were used to fit the reference curve. The worst standard error is obtained by the MS method in both experiments ($\hat{\boldsymbol{h}}_{\mathrm{MS}}$). The best standard error, apart from the result with close-up data, is obtained with the data produced by one human experimenter, which is however different in each experiment ($\hat{\boldsymbol{h}}_{\mathrm{VS1}}$, $\hat{\boldsymbol{h}}_{\mathrm{VS2}}$). In each experiment, the SCS-based SBH data ($\hat{\boldsymbol{h}}_{\mathrm{SCS}}$) leads to a standard error that is smaller than one of the standard errors obtained by the human experimenters.

The curve-fitting is also executed for the other experiments by using the SBH profiles obtained the MS and SCS methods. Table 3 lists the obtained coefficients of determination (R^2). One can see that R^2 is above 0.995 in all cases except for the MS method, which delivers R^2 values as low as 0.235. This means that the SBH measurement profiles satisfy the expected concave-convex shape very well, except for the profiles obtained with the MS method. The corresponding SBH profiles ($\hat{\boldsymbol{h}}_{\mathrm{MS}}$) and the fitted curves are displayed in the *Supplementary Information*. Visual inspection allows to conclude that the MS method remains extremely sensitive to noise. Indeed, the MS method frequently identifies pixels that are close to the bottom of the image due to the high noise in the computed slopes. Several tests were executed to evaluate whether the considered set of pixels could be expanded or reduced (above/below 1225 pixels). However, in the 8th and 9th experiment the sludge blanket at the end of the experiment is located close to the 1225th pixel so that further decreases are difficult to motivate. At the same time, the results for experiment 1 show sensitivity to noise at the start of the experiment. Expanding the considered pixel selection makes things even worse. It is therefore impossible to define a single set of top-most pixels to be considered in the MS method in such a way that low sludge blanket levels can be identified while also avoiding errors due to noise amplification for pixels close to reference pixel at the bottom of the images. Given such poor performance, further analysis excludes results on the basis of the MS method.

3.4. Zone Settling Velocity Estimation

As indicated above, computing the ZSV is one way to usefully interpret the obtained SBH profiles. The curve fitting described above identifies the location of the inflection point at the concave-convex intersection of the SBH profile. As is typically assumed, the ZSV corresponds to the slope of the tangent in the inflection point located at the transition from the concave to the convex episode. In experiment 1 to 8, the obtained tangent lines appear sensible based on visual inspection (see Fig. 5 and the *Supplementary Information*. For experiment 9 the time needed for the transition from the zone settling phase to the compressed settling phase is extremely short which likely affects the accuracy of the estimated slope of the tangent line, as also discussed in van Loosdrecht et al. (2016).

All slopes of the identified tangent lines correspond to settling velocities and are shown in the top panel of Fig. 6. As expected, the obtained settling velocities follow a decreasing concave trend. In addition, the results obtained with visual estimates are generally consistent with the SCS-based results (maximum 27% relative difference). A conclusive validation would however require additional samples. A fit of the Vesilind equation ($v(c) = v_0\ e^{-r_v\ c}$, with c the sludge concentration, $v(c)$ the ZSV, and v_0 and r_v parameters) is shown as well and delivers an R2 value of 0.95. As an alternative, a fit of a rational equation (Eq. 28, Diehl, 2015) is also shown. This rational equation has three parameters and delivers an R2 value of 0.86. Both equations thus fit the data well and cannot not be discriminated easily. The bottom panel shows the corresponding settling flux ($q(c) = v(c) \cdot c$) which is typically used for the determination of the settling capacity of secondary settlers. Note that the Vesilind and rational equations are designed to describe the settling behavior at relatively high concentrations where zone settling occurs. It is therefore not surprising that the curves have a different shape in the low concentration region.

4. Discussion

4.1. Main Results and Major Benefits of the Proposed Method

Image analysis was executed for the first time by means of a method for qualitative trend analysis, particularly on the basis of an SCS model. Furthermore, automated SBH registration is benchmarked for the first time against a pre-existing image analysis method for SBH registration and conventional SBH registration by human experimenters. Based on our results, several benefits of the proposed method when applied for image analysis during batch settling experiments have been demonstrated:

- The images were obtained with an off-the-shelf digital camera, all code is released publicly, and both experiments and image analysis can be executed in a standard laboratory environment. Consequentially, the method is accessible to many in the field, in contrast to alternatives which rely on equipment and software that is expensive to obtain and maintain.

- The SCS data model allows automatic SBH estimation based on light intensity profiles extracted from digital images recorded during batch settling experiments. As demonstrated, this is also possible despite the collection of rather noisy images. In contrast, the pre-existing maximum slope (MS) method is very sensitive to noise. Because of this, we expect our method to fare well even in cases where the supernatant remains turbid, e.g. when pin-point flocs are present.

- The SCS data model fits curves to the complete light intensity profiles and all color channels at once. Put otherwise, *(i)* all available information is incorporated in the image analysis, *(ii)* noise amplification due to differentiation is avoided, and *(iii)* information removal and biasing effects of data filtering are absent.

- The combined experimental and data-analytic method prevents human error and subjective analysis by automating the SBH registration via deterministic optimization. In contrast, conventional approaches may suffer from uncertainty stemming from subjectivity of human experimenters as well as variability of the exact method. Such variability may stem from the application of different practices in different regions, in individual wastewater treatment plants, by individual operators, and over time.

In its current form, our image-based analysis is considered attractive to academic experimenters primarily as a way to increase the efficiency of experimental data collection, possibly enabling the execution of measurement campaigns over long periods or with a high measurement frequency. It may also be useful in full-scale activated sludge WWTPs where an early-stage warning of deteriorating sludge settling properties is warranted. Importantly, routine application requires as much sample preparation as is necessary to obtain the diluted sludge settling index (DSVI) given that the time spent on sludge blanket registration with the human eye can be omitted.

At the same time, our results lead to acceptable but still considerable deviations between the results obtained with the SCS-method and those obtained with human-eye based SBH profiles. The number of experiments executed to develop and demonstrate the SCS-method are however too low to establish whether the observed deviations are of a systematic or random nature. In addition, it is unclear whether the larger errors should be expected in the human-eye SBH profiles or the SCS-based profiles. Our initial experiences suggest that human-eye SBH profiles can exhibit some lag during the time zone-settling dominates, especially when the sludge blanket is not defined well yet. Indeed, the fast-forming and fast-moving sludge blanket can be hard to track in time by the human eye. Regardless of such differences, the SCS-based method also offers the ability to obtain an objective SBH reading rather than a reading prone to human error and subjectivity.

4.2. Expanded Range of Qualitative Trend Analysis Applications

Historically speaking, qualitative trend analysis methods, including the original SCS method, were proposed to tackle extrapolation issues in fault diagnosis (see e.g. Maurya et al., 2007; Villez et al., 2013). Recent work expanded the range of applicability of such methods to fault detection in sequencing batch reactors (Villez and Habermacher, 2016), ammonia control (Thürlimann et al., 2015) and dynamic model identification (Mašić et al., 2017). SCS-based data modeling is especially valuable when models which are entirely mechanistic in nature are prohibitively expensive to obtain. The current study expands the application range of the SCS data model further into the field of image analysis and characterization of separation processes. Thus, our current results further demonstrate the general applicability of qualitative trend analysis methods and SCS-based methods in particular.

4.3. Perspectives

Given the promising results in this study, several new questions can be raised. The following topics are of primary interest:

1. Is the image analysis method robust enough to handle several sludge types without further modification?
2. Can the image analysis method also be used for experimentation with highly diluted sludges whose settling is of Stokesian nature?
3. Are the obtained SBH profiles useful for more complex modeling tasks such as the joint modeling of hindered and compressed settling? This may be the case but it is unclear yet whether the SCS-based SBH profiles are of sufficient quality.
4. Can the time savings obtained by avoiding human-eye sludge blanket reading be increased further by enabling the execution of multiple simultaneous settling experiments and/or by providing a sludge sample preparation device that does not modify the flocculation state? If possible, the SBH registration method combined with automated sample preparation will finally enable the evaluation of predictive control strategies based on solid flux theory, including automated control of the recycle flow rate, step feed flow rate, step sludge flow rates, and temporary sedimention in aeration tanks.

Based on current experience the authors are convinced that the answer to each of the above questions is yes. However, further experimental evidence is warranted. In any case, our experiments suggest that the desired experimental evidence can now be collected in an objective and time-efficient manner.

5. Conclusions

Automatic registration of the sludge blanket height in settling experiments is demonstrated to be feasible via image analysis. The image analysis procedure is based on a multivariate extension of the shape constrained spline method. Promising results were obtained with inexpensive equipment accessible to any laboratory. It is especially noteworthy that the shape constrained splines method appears fairly robust against large levels of noise and the obtained results compare fairly to conventional sludge blanket height registration methods. Most importantly, we consider our study the first step towards a fully automated, reliable, and economical alternative to existing methods for sludge blanket height registration.

6. Acknowledgments

This work was supported by the Commission for Technology and Innovation (CTI) of the Swiss Federal Department of Economic Affairs Education and Research (EAER) (CTI project no. 14351.1 PFIW-IW). The authors thank Gustaf Olsson for sparking our interest in the topic and feedback. We thank Stefan Diehl, Ulf Jeppsson, and Eberhard Morgenroth for their comments and suggestions. All computations were executed by joint use of Matlab (The MathWorks Inc., 2014); the Functional Data Analysis software package accompanying the book (Ramsay and Silverman, 2002); and MOSEK (Andersen and Andersen, 2000; MOSEK ApS, 2012).

7. References

Andersen, E. D., Andersen, K. D., 2000. The MOSEK interior point optimizer for linear programming: an implementation of the homogeneous algorithm. High Performance Optimization 33, 197–232.

Balslev, P., Nickelsen, C., Lynggaard-Jensen, A., 1994. On-line flux-theory based control of secondary clarifiers. Water Science and Technology 30 (2), 209–218.

Bredeweg, B., Linnebank, F., Bouwer, A., Liem, J., 2009. Garp3 – Workbench for qualitative modelling and simulation. Ecological Informatics 4(5), 263–281.

Bürger, R., Diehl, S., 2013. Convexity-preserving flux identification for scalar conservation laws modelling sedimentation. Inverse Problems 29 (4), 045008.

Bye, C. M., Dold, P. L., 1998. Sludge volume index settleability measures: effect of solids characteristics and test parameters. Water Environment Research 70 (1), 87–93.

Cacossa, K. F., Vaccari, D. A., 1994. Calibration of a compressive gravity thickening model from a single batch settling curve. Water Science and Technology 30 (8), 107–116.

CHDK, 2016.
URL `http://chdk.wikia.com`

Chen, J., Beck, M. B., 2001. Operational control of storm sewage at an activated sludge process. Water Science and Technology 43 (7), 131–137.

Daigger, G. T., Roper Jr, R. E., 1985. The relationship between SVI and activated sludge settling characteristics. Water Pollution Control Federation Journal, 859–866.

De Clercq, J., 2006. Batch and continuous settling of activated sludge: in-depth monitoring and 1D compression modelling. Ph.D. thesis, Ghent University.

De Clercq, J., Jacobs, F., Kinnear, D. J., Nopens, I., Dierckx, R. A., Defrancq, J., Vanrolleghem, P. A., 2005. Detailed spatio-temporal solids concentration profiling during batch settling of activated sludge using a radiotracer. Water Research 39 (10), 2125–2135.

Diehl, S., 2007. Estimation of the batch-settling flux function for an ideal suspension from only two experiments. Chemical Engineering Science 62 (17), 4589–4601.

Diehl, S., 2015. Numerical identification of constitutive functions in scalar nonlinear convection-diffusion equations with application to batch sedimentation. Applied Numerical Mathematics 95, 154–172.

Ekama, G. A., Barnard, J. L., Gunthert, F. W., Krebs, P., McCorquodale, J. A., Parker, D. S., Wahlberg, E. J., 1997. Secondary settling tanks: theory, modelling, design and operation. Scientific and technical report no. 6. International Association on Water Quality, London, UK.

Hastie, T., Tibshirani, R., Friedman, J., 2001. The elements of statistical learning. Data Mining, Inference, and Prediction. Springer, NY, USA.

Kim, Y. J., Choi, S. J., Bae, H., Kim, C. W., 2011. Sludge settleability detection using automated SV30 measurement and its application to a field WWTP. Water Science and Technology 64 (8), 1743–1749.

Kuipers, B. J., 1994. Qualitative Reasoning: Modeling and simulation with incomplete knowledge. MIT Press, Cambridge, MA, USA.

Li, B., Stenstrom, M. K., 2014. Research advances and challenges in one-dimensional modeling of secondary settling tanks – a critical review. Water Research 65, 40–63.

Li, B., Stenstrom, M. K., 2016. Practical identifiability and uncertainty analysis of the one-dimensional hindered-compression continuous settling model. Water Research 90, 235–246.

Locatelli, F., François, P., Laurent, J., Lawniczak, F., Dufresne, M., Vazquez, J., Bekkour, K., 2015. Detailed velocity and concentration profiles measurement during activated sludge batch settling using an ultrasonic transducer. Separation Science and Technology 50 (7), 1059–1065.

Mancell-Egala, W. A., Kinnear, D. J., Jones, K. L., De Clippeleir, H., Takács, I., Murthy, S. N., 2016. Limit of stokesian settling concentration characterizes sludge settling velocity. Water Research 90, 100–110.

Maurya, M. R., Rengaswamy, R., Venkatasubramanian, V., 2007. Fault diagnosis using dynamic trend analysis: A review and recent developments. Engineering Applications of Artificial Intelligence 20, 133–146.

Mašić, A., Srinivasan, S., Billeter, J., Bonvin, D., Villez, K., 2017. Shape constrained splines as transparent black-box models for bioprocess modeling. Computers and Chemical Engineering 99 (6), 96–105.

Mines Jr, R. O., Vilagos, J. L., Echelberger Jr, W. F., Murphy, R. J., 2001. Conventional and AWT mixed-liquor settling characteristics. Journal of Environmental Engineering 127 (3), 249–258.

MOSEK ApS, 2012. MOSEK Optimization Software for MATLAB, Version 6.0. Available from http://www.mosek.com/.

Ozinsky, A. E., Ekama, G. A., 1995a. Secondary settling tank modelling and design. Part 1: Review of theoretical and practical developments. Water S. A. 21 (4), 325–322.

Ozinsky, A. E., Ekama, G. A., 1995b. Secondary settling tank modelling and design. Part 2: linking sludge settleability measures. Water S. A. 21 (4), 333–349.

Papp, D., 2011. Optimization models for shape-constrained function estimation problems involving nonnegative polynomials and their restrictions. Ph.D. thesis, Rutgers University, New Brunswick, NJ, USA.

Papp, D., Alizadeh, F., 2014. Shape-constrained estimation using nonnegative splines. Journal of Computational and Graphical Statistics 23, 211–231.

Plósz, B. G., Weiss, M., Printemps, C., Essemiani, K., Meinhold, J., 2007. One-dimensional modelling of the secondary clarifier-factors affecting simulation in the clarification zone and the assessment of the thickening flow dependence. Water Research 41 (15), 3359–3371.

Ramin, E., Wágner, D. S., Yde, L., Binning, P. J., Rasmussen, M. R., Mikkelsen, P. S., Plósz, B. G., 2014. A new settling velocity model to describe secondary sedimentation. Water Research 66, 447–458.

Ramsay, J. O., Silverman, B. W., 2002. Applied Functional Data Analysis: Methods and Case Studies. Springer, New York, NY, USA.

Ramsay, J. O., Silverman, B. W., 2005. Functional Data Analysis. Springer, New York, NY, USA.

Shaich, D., Becker, R., King, R., 2001. Qualitative modelling for automatic identification of mathematic models of chemical reaction systems. Control Engineering Practice 9, 1373–1381.

The MathWorks Inc., 2014. MATLAB Release 2014b. Natick, MA, USA.

Thürlimann, C. M., Dürrenmatt, D. J., Villez, K., 2015. Qualitative trend analysis for pH based soft-sensing of ammonia in full scale continuous WWTPs. Proceedings of the 2nd IWA New Developments in IT & Water conference Rotterdam, The Netherlands (February 8-10, 2015), appeared on USB–stick.

Torfs, E., Locatelli, F., Balemans, S., Laurent, J., Vanrolleghem, P. A., Bürger, R., Diehl, S., François, P., Mosse, R., Nopens, I., 2016. Concentration-driven models revisited: Towards a unified framework to model settling tanks in WWTPs. In: Proceedings 5th IWA/WEF Wastewater Treatment Modelling Seminar (WWTmod2016). Annecy, France, April 2-6, 2016. 109-118.

Traoré, A., Grieu, S., Thiery, F., Polit, M., Colprim, J., 2006. Control of sludge height in a secondary settler using fuzzy algorithms. Computers and Chemical Engineering 30 (8), 1235–1242.

van Loosdrecht, M. C., Nielsen, P. H., Lopez-Vazquez, C. M., Brdjanovic, D., 2016. Experimental methods in wastewater treatment. Water Intelligence Online 15 (9781780404752).

Vanderhasselt, A., Vanrolleghem, P. A., 2000. Estimation of sludge sedimentation parameters from single batch settling curves. Water Research 34 (2), 395–406.

Vanrolleghem, P., Van der Schueren, D., Krikilion, G., Grijspeerdt, K., Willems, P., Verstraete, W., 1996. On-line quantification of settling properties with in-sensor-experiments in an automated settlometer. Water Science and Technology 33 (1), 37–51.

Vanrolleghem, P. A., Clercq, B. D., Clercq, J. D., Devisscher, M., Kinnear, D. J., Nopens, I., 2006. New measurement techniques for secondary settlers: a review. Water Science and Technology 53 (4-5), 419–429.

Vesilind, P. A., 1968. Design of prototype thickeners from batch settling tests. Water Sewage Works 115, 302–307.

Villez, K., Habermacher, J., 2016. Shape anomaly detection for process monitoring of a sequencing batch reactor. Computers and Chemical Engineering 91, 365–379.

Villez, K., Venkatasubramanian, V., Rengaswamy, R., 2013. Generalized shape constrained spline fitting for qualitative analysis of trends. Computers and Chemical Engineering 58, 116–134.

Table 1: List of batch settling experiments. Experiments marked with $^{(*)}$ are those experiments for which visual registration of the sludge blanket height was performed by two human experimenters (during the experiment) and by visual inspection of close-up images (after the experiment).

Experiment index	Original sludge sample	Concentration g/L	Pixel height J
1	1	2.40 (no dilution)	1275
2	1	1.92	1282
3	1	1.54	1285
4	1	1.22	1285
5 $^{(*)}$	2	1.20	1286
6 $^{(*)}$	2	1.00	1287
7	2	0.86	1289
8	2	0.74	1279
9	2	0.58	1287

Table 2: Standard error (in mL) obtained by considered the deviations between the SBH measurements and the curve fitted to the SBH measurement obtained by close-up image inspection (VO).

Experiment index	Method				
	SCS	MS	VO	VS1	VS2
5	18.3	37.9	2.51	7.37	32.6
6	23.9	36.3	5.19	41.1	21.5

Table 3: Coefficients of determination (R^2) for the curves fitted to each of the sludge blanket height profiles.

Experiment index	Method				
	SCS	MS	VO	VS1	VS2
1	0.9999	0.5607			
2	0.9999	0.9972			
3	0.9999	0.8036			
4	0.9997	0.8795			
5	0.9998	0.9972	1.0000	1.0000	0.9975
6	0.9990	0.9989	0.9994	0.9998	1.0000
7	0.9993	0.8027			
8	0.9990	0.8580			
9	0.9954	0.2353			

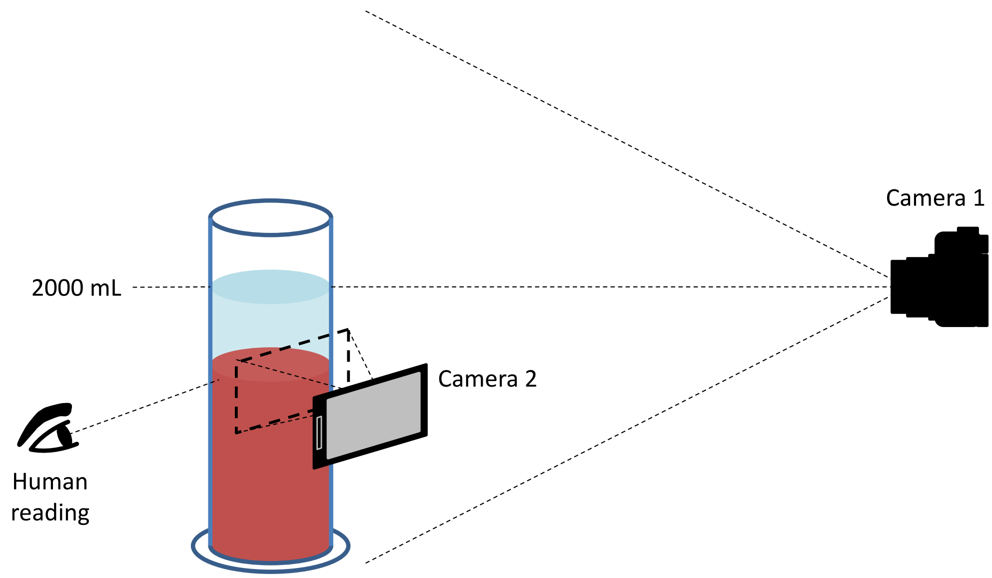

Figure 1: Scheme of the experimental setup. Camera 1 is positioned level to the top surface of the sludge sample. Camera 2 is adjusted manually during each experiment to take close-up images of the sludge blanket. Human inspection is executed in such a way that the lines of sight of the cameras are not interrupted.

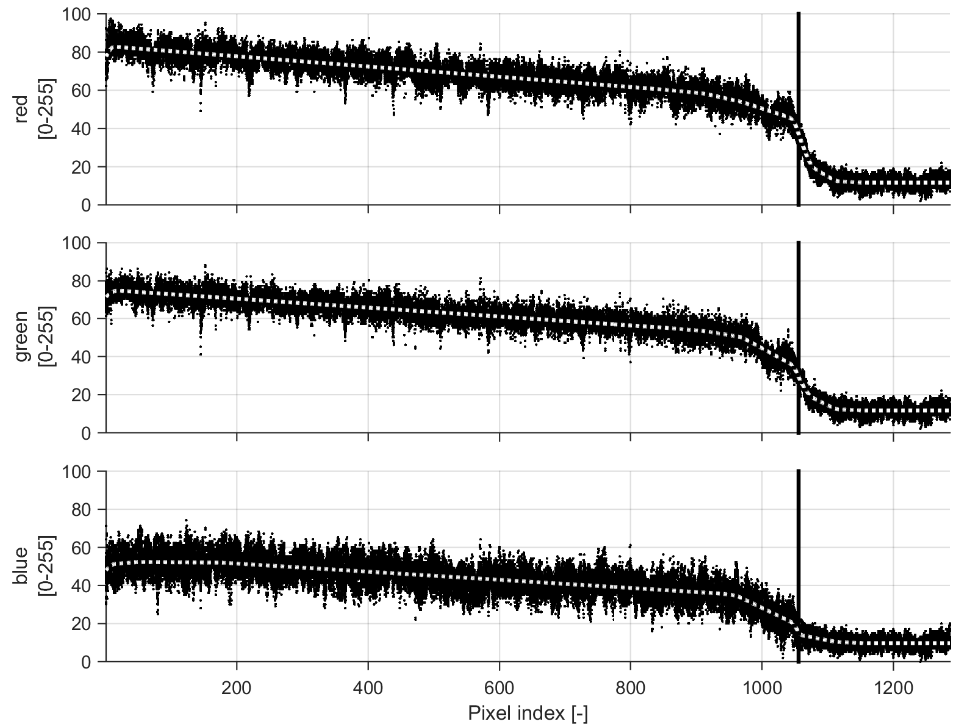

Figure 2: Experiment 5 - Image 42. Dots: Light intensity data; Dashed white lines: Fitted shape-constrained spline functions; Full black vertical lines: Identified inflection point location. The shape constrained splines method located the inflection point in the light intensity data successfully and is consistent with a visual assessment of the sludge blanket height.

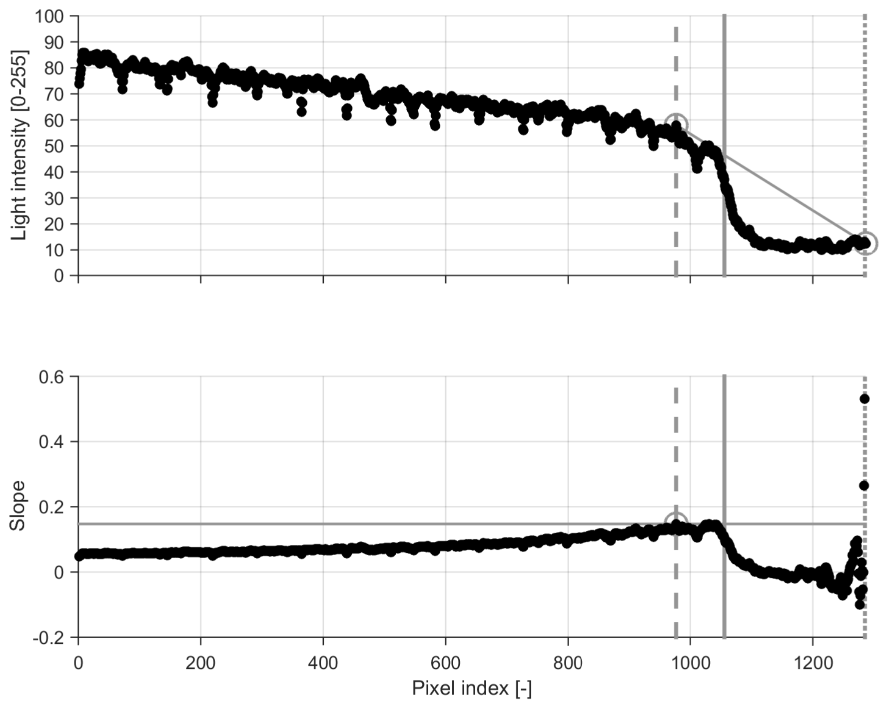

Figure 3: Experiment 5 - Image 42. (Top) Dots: Averaged red channel light intensity data; Dotted vertical line: Pixel location obtained with maximal slope method considering every pixel; Dashed vertical line: Pixel location obtained with maximal slope method considering only the first 1225 pixels; Full vertical line: Pixel location obtained via shape-constrained spline function fitting; Circles and connecting full line: vizualization of the maximal slope when considering only the first 1225 pixels. (Bottom) Dots: Computed slopes; Dotted vertical line: Pixel location obtained with maximal slope method considering every pixel; Dashed vertical line: Pixel location obtained with maximal slope method considering only the first 1225 pixels; Full vertical line: Pixel location obtained via shape-constrained spline function fitting; Circles and horizontal full line: vizualization of the maximal slope when considering only the first 1225 pixels. The maximum slope method delivers results that are fairly different from the result obtained with the shape constrained splines method.

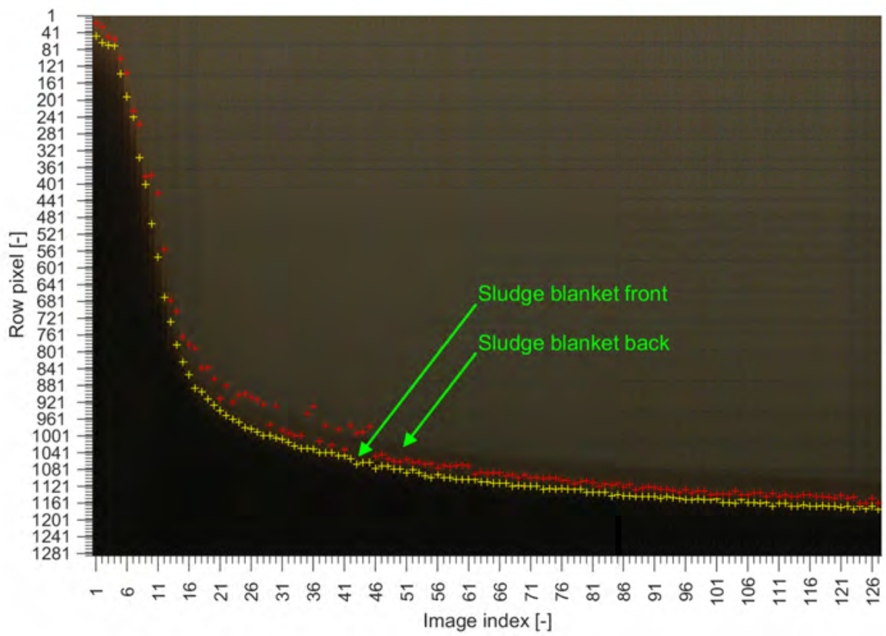

Figure 4: Experiment 5. Composite image showing data from 127 consecutive images. Green arrows are used to indicate the sludge blanket at the front and back of the column recognized by close visual inspection. Yellow cross-hairs indicate the sludge blanket height estimates obtained by means of the shape constrained splines method and correspond to the front of the column. Red cross-hairs indicate the sludge blanket height estimates obtained by means of the maximum slope method. The red cross-hairs do not match any obvious feature in the image and follow an irregular pattern.

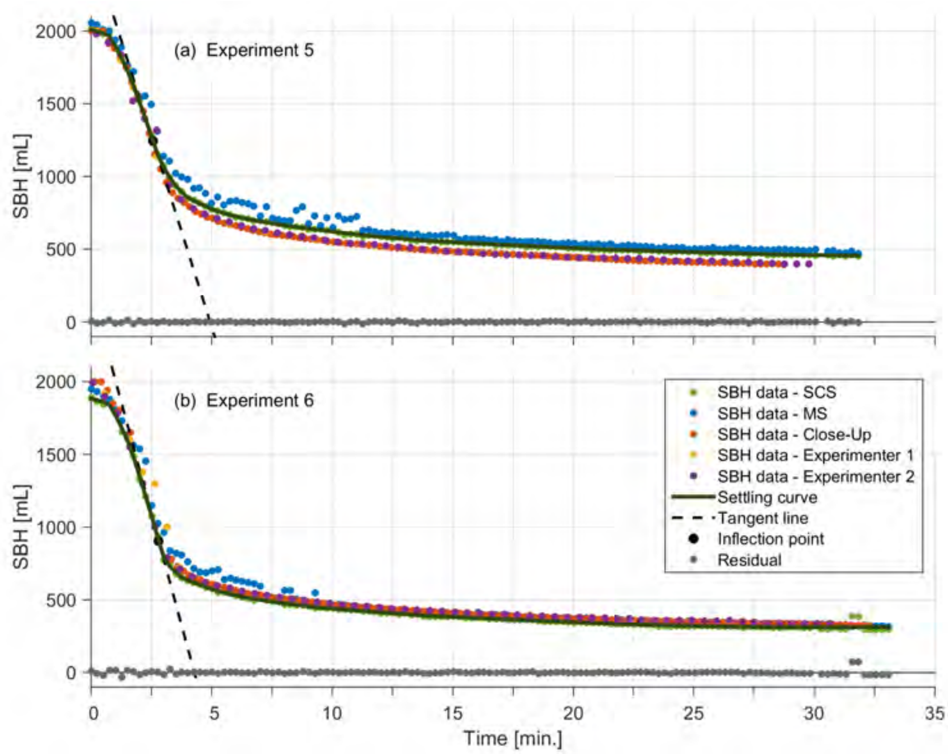

Figure 5: Registered batch settling curves: *Top*: Experiment 5; *Bottom*: Experiment 6. SCS-based sludge blanket height profiles (green dots, $\hat{\boldsymbol{h}}_{\mathrm{SCS}}$), MS-based sludge blanket height profiles (blue dots, $\hat{\boldsymbol{h}}_{\mathrm{MS}}$) and profiles based on visual registration (red, yellow, and purple dots; $\hat{\boldsymbol{h}}_{\mathrm{VO}}$, $\hat{\boldsymbol{h}}_{\mathrm{VS1}}$, and $\hat{\boldsymbol{h}}_{\mathrm{VS2}}$). A spline function with a concave-convex shape (full grey line) is fitted to the $\hat{\boldsymbol{h}}_{\mathrm{SCS}}$ data (SBH data - SCS). The tangent line in the inflection point of the shape constrained splines function is shown with a dashed black line. The modeling errors (grey circles) show that the curve fits the data well in both experiments.

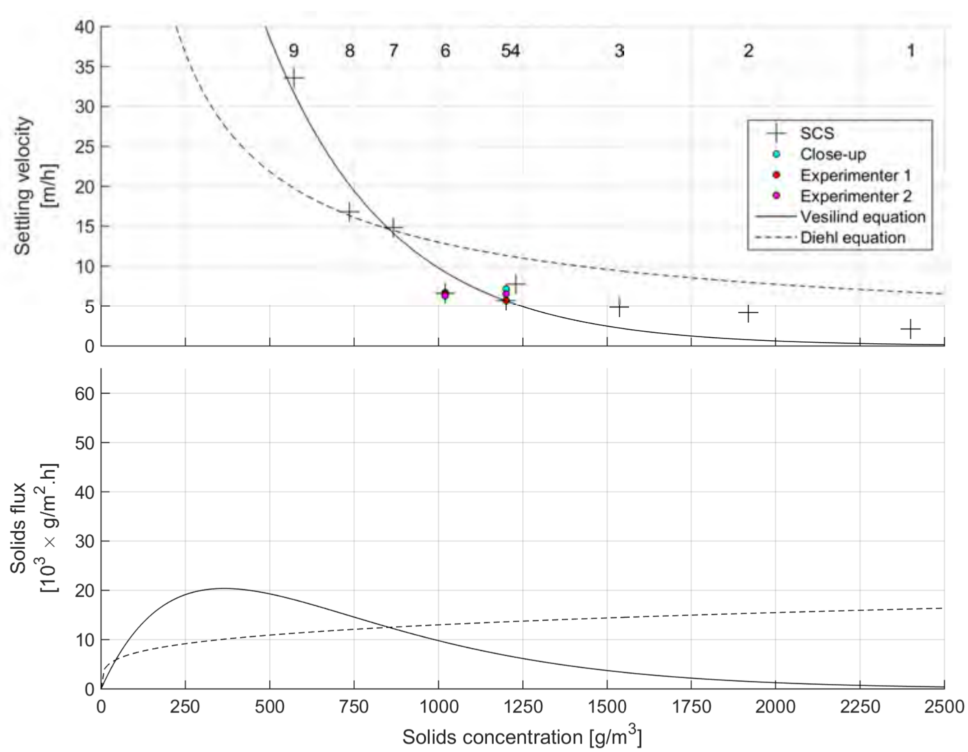

Figure 6: Use of the ZSV to characterize dynamic sludge settling properties. *Top:* Zone settling velocity (ZSV) as a function of the sludge concentration. All ZSVs are shown together with a least-squares fit of the Vesilind and Diehl equations. The experiment number is added at the top of the image right above the corresponding solids concentration. *Bottom:* Settling flux curve obtained based on the fitted Vesilind and Diehl equations.

S. Supplementary Information

The Supplementary Information includes additional details regarding the experimental method (Section S.1), the SCS modeling method (Section S.2), additional figures (Section S.3), and all data and software to reproduce our results (separate .zip file).

S.1. Experimental protocol

The following description of a single experiment is added to ensure broad applicability of the SCS-based SBH registration method.

S.1.1. Hardware and consumables

Prior to the experiment, collect and prepare the following materials:

1. A 2 L clear glass cylinder with coloured tape added to mark the 200 mL and 1000 mL levels. Take note of the distance between these two levels.
2. A white panel to place behind the 2 L cylinder.
3. An off-the-shelf digital camera, equipped with a continuous power supply and programmed to continuously collect an image at a fixed time interval.
4. A diluted sludge sample of at least 2 L with known solids concentration.
5. A stirring rod

S.1.2. Protocol

Execute the following steps in the laboratory:

1. Place the camera, cylinder, and panel on a single line on a horizontal platform.

2. Position the camera so that the line-of-sight corresponds to a horizontal line aligned with the 2000 mL mark on the cylinder.
3. ensure that the positions of the camera, cylinder, and panel do not change during the experiment.
4. Start the image collection program on the camera.
5. Fill the cylinder with the 2 L of the diluted sludge sample.
6. Stir the sample with the stirring rod.
7. Stop stirring right before the recording of an image and record the time stirring was halted.
8. Let the sludge settle for as long as considered necessary (e.g., 30 minutes).
9. Stop the image collection program on the camera.
10. Empty and clean the cylinder.

The following steps are executed after the experiment is executed.

1. Collect all images from the camera.
2. Select all images of interest starting with the image where stirring was stopped first.
3. Select a section in the images corresponding to the center of the cylinder and covering the 200 mL to 2000 mL range of the column.
4. Apply the SCS method to find the pixel corresponding to the sludge blanket in an image section. Apply this to every image section.
5. Convert the sludge blanket pixels to a sludge blanket height (SBHs) by linear interpolation.

S.2. Description and proofs of applied bounding procedures

In the next paragraphs, the necessary elements contributing to the globally optimal solution of the SCS optimization problem discussed in the text are explained in detail. Additional symbols not used in the main text are given in Table S.1.

Table S.1: List of symbols used only within the Supplementary Information

Symbol	Definition
$\boldsymbol{\beta}^{\mathrm{L}}$	Lower bound values for of all spline function coefficients
$\boldsymbol{\beta}^{\mathrm{U}}$	Upper bound values for of all spline function coefficients
ϵ	Bounding gap tolerance
$\underline{\theta_t}$	Lower bound for θ_t
$\overline{\theta_t}$	Upper bound for θ_t
$\boldsymbol{\theta}_{QP}$	Upper bound solution for $\boldsymbol{\theta}$
Θ_l	lth considered set for $\boldsymbol{\theta}$ during optimization
$\underline{g}$	Lower bound to the objective function
$\overline{g}$	Lower bound to the objective function

The complete optimization problem is written as follows:

$$\hat{\boldsymbol{\beta}}, \hat{\boldsymbol{\theta}} = \arg\min_{\boldsymbol{\beta}, \boldsymbol{\theta}} g(\boldsymbol{\beta}, \boldsymbol{\theta}) = \sum_{j=1}^{J} \sum_{k=1}^{K} \left(\tilde{\boldsymbol{Y}}_{j,k} - \boldsymbol{Y}_{j,k}(\boldsymbol{\beta}) \right)^2 \tag{S.1}$$

$$\text{s.t.} \quad \forall k = 1, \ldots, K :$$

$$\boldsymbol{Y}(\boldsymbol{\beta}) = \boldsymbol{f}(\boldsymbol{\beta}, \boldsymbol{x}_k) \tag{S.2}$$

$$\boldsymbol{\beta} \in \Omega(\boldsymbol{\theta}, \boldsymbol{S}) \tag{S.3}$$

$$\boldsymbol{\theta} \in \Theta \tag{S.4}$$

S.2.1. Solving for $\boldsymbol{\beta}$

The SCS function fitting problem discussed in the main text is a pseudo-convex program as long as values for the transitions ($\boldsymbol{\theta}$) are fixed and known. Depending on the applied sign constraints and the exact objective function, the problem can be reduced to a semi-definite program, a second order cone program, or even a quadratic program (QP). This is discussed at length in Papp (2011); Villez et al. (2013); Papp and Alizadeh (2014).

S.2.2. Solving for $\boldsymbol{\beta}$ *and* $\boldsymbol{\theta}$

The original problem described in the main text requires simultaneous optimization of the transitions $\boldsymbol{\theta}$. This is a nonlinear problem. However, and similar to prior work, this kind of problem can be solved to global optimality in a deterministic manner by means of the branch-and-bound algorithm (Villez et al., 2013). To this end, the algorithm repeatedly divides the set of feasible values for $\boldsymbol{\theta}$ (Θ) into smaller subsets until convergence. We refer to the lth generated subset during algorithm execution as Θ_l ($\Theta_l \subset \Theta$). For each subset, a lower and upper bound value to the objective function is computed. These bounds allow ignoring branches in the resulting solution tree during the remainder of the optimization algorithm execution as soon as it is guaranteed that those branches cannot include the global optimum. The exclusion of such branches from the algorithmic search is known as *fathoming*. In what follows, the bounding procedures enabling such fathoming are explained and proven.

S.2.2.1. Step 1: Finding a feasible solution for $\boldsymbol{\theta}$*.* Consider a candidate solution set, Θ_l. Any such set corresponds to a hyper-rectangular set within the feasible solution space and can be described completely as follows:

$$\boldsymbol{\theta} \in \Theta_l \Leftrightarrow \forall t \in \{1, 2, \ldots, T\} : \quad \underline{\theta_t} \leq \theta_t \leq \overline{\theta_t} \tag{S.5}$$

with $\underline{\theta_t}$ and $\overline{\theta_t}$ describing the interval containing the considered values for θ_t.

In addition, each feasible solution within this set satisfies the following order relationship:

$$\forall t \in \{1, 2, \ldots, T-1\} : \theta_t \leq \theta_{t+1} \tag{S.6}$$

A practical way to propose a feasible solution is obtained by solving the following QP subject to the above conditions (Eq. S.5–S.6):

$$\min_{\boldsymbol{\theta}} \sum_{t=1}^{T} (\theta_t - \underline{\theta_t})^2 + (\theta_t - \overline{\theta_t})^2 \tag{S.7}$$

The solution, if the problem is feasible, is further referred to as $\boldsymbol{\theta}^{\mathrm{QP}}$. If the set defined by Eq. S.5–S.6 is empty, one cannot find a feasible solution. This case is dealt with separately.

S.2.2.2. Step 2a: No feasible solution available. When no feasible solution for $\boldsymbol{\theta}$ can be found, the bounding procedures are trivial.

Procedure. In this case, the bounding procedures are very straightforward. As in prior work, both the upper bound $(\overline{g(\Theta_l)})$ and lower bound $(\underline{g(\Theta_l)})$ are set to $+\infty$:

$$\underline{g} = \underline{g(\Theta_l)} = \overline{g} = \overline{g(\Theta_l)} = +\infty \tag{S.8}$$

Proof. The proof of these bounds is straightforward. Indeed, if no feasible solution can be found $\boldsymbol{\theta}$, then there no solution can be found with any objective function value lower than $+\infty$. This automatically also defines the upper bound at the same value. This concludes the proof.

S.2.2.3. Step 2b: A feasible solution is found. Computing the upper and lower bounds is more involved when a feasible solution for $\boldsymbol{\theta}$, namely $\boldsymbol{\theta}^{\mathrm{QP}}$, has been found.

Upper bound – Procedure. An upper bound value for the objective function is computed by replacing $\boldsymbol{\theta}$ with the proposed solution $(\boldsymbol{\theta}^{\mathrm{QP}})$ in the original problem (Eq. S.1–S.4). This means the following problem is now solved:

$$\hat{\boldsymbol{\beta}}^{\mathrm{U}} = \arg\min_{\boldsymbol{\beta}} \overline{g(\boldsymbol{\beta})} = \sum_{j=1}^{J}\sum_{k=1}^{K}\left(\tilde{\boldsymbol{Y}}_{j,k} - \boldsymbol{Y}_{j,k}(\boldsymbol{\beta})\right)^2 \tag{S.9}$$

$$\text{s.t.} \quad \forall k = 1, \ldots, K:$$

$$\boldsymbol{Y}(\boldsymbol{\beta}) = \boldsymbol{f}(\boldsymbol{\beta}, \boldsymbol{x}_k) \tag{S.10}$$

$$\boldsymbol{\beta} \in \Omega(\boldsymbol{\theta}^{\mathrm{QP}}, \boldsymbol{S}) \tag{S.11}$$

This problem is again at least pseudo-convex and can thus be solved to deterministic global optimality by means of interior-point algorithms. The corresponding vector containing all spline coefficients is referred to as $\hat{\boldsymbol{\beta}}^{\mathrm{U}}$. The resulting objective function is an upper bound to the objective function:

$$\exists \boldsymbol{\theta} \in \Theta_l, \exists \boldsymbol{\beta} \in \Omega(\Theta_l, \boldsymbol{S}) : g(\boldsymbol{\beta}, \boldsymbol{\theta}) \leq \overline{g} = \overline{g\left(\hat{\boldsymbol{\beta}}^{\mathrm{U}}\right)} \tag{S.12}$$

Upper bound – Proof. Any feasible solution, including the computed pair $(\boldsymbol{\beta}^{\mathrm{U}}, \boldsymbol{\theta}^{\mathrm{QP}})$, corresponds to an upper bound as its existence automatically implies that at least one solution exists which delivers an objective function value which is the same or lower value than the computed one, $g(\boldsymbol{\beta}^{\mathrm{U}}, \boldsymbol{\theta}^{\mathrm{QP}})$. As such, this proves the validity of the computed upper bound.

Lower bound – Procedure. A lower bound can be computing by means of the following relaxation of the problem. For the considered subset Θ_l, one applies only those sign constraints which are applied universally for all solutions $\boldsymbol{\theta}$ within the set Θ_l. Practically, the original problem is relaxed by replacing the instances of θ_t with either $\underline{\boldsymbol{\theta}}$ or $\overline{\boldsymbol{\theta}}$ as follows:

$$\hat{\boldsymbol{\beta}} = \arg\min_{\boldsymbol{\beta}} \underline{g(\boldsymbol{\beta})} = \sum_{j=1}^{J}\sum_{k=1}^{K}\left(\tilde{\boldsymbol{Y}}_{j,k} - \boldsymbol{Y}_{j,k}(\boldsymbol{\beta})\right)^2 \tag{S.13}$$

$$\text{s.t.} \quad \forall k = 1, \dots, K :$$

$$\boldsymbol{Y}(\boldsymbol{\beta}) = \boldsymbol{f}(\boldsymbol{\beta}, \boldsymbol{x}_k) \tag{S.14}$$

$$\boldsymbol{\beta} \in \Omega^{\mathrm{L}}(\underline{\boldsymbol{\theta}}, \overline{\boldsymbol{\theta}}, \boldsymbol{S}) \tag{S.15}$$

where $\Omega^{\mathrm{L}}(\underline{\boldsymbol{\theta}}, \overline{\boldsymbol{\theta}}, \boldsymbol{S})$ is the relaxed feasible set for $\boldsymbol{\beta}$, which is defined as follows:

$$\begin{aligned}
&\boldsymbol{\beta} \in \Omega^{\mathrm{L}}(\underline{\boldsymbol{\theta}}, \overline{\boldsymbol{\theta}}, \boldsymbol{S}) \\
&\qquad \Updownarrow \\
&\forall d = 0, \dots, D_k,\ \forall e = 1, \dots, E,\ \forall t = 1, \dots, T,\ \forall k = 1, \dots, K : \\
&\quad f_k^{(d)}(\boldsymbol{\beta}_k, x) \begin{cases} \geq 0 \ \text{ if } \ \underline{b_e} \leq x \leq \overline{b_e} \wedge s_{e,d+1} = +1 \\ = 0 \ \text{ if } \ \underline{b_e} \leq x \leq \overline{b_e} \wedge s_{e,d+1} = 0 \\ \leq 0 \ \text{ if } \ \underline{b_e} \leq x \leq \overline{b_e} \wedge s_{e,d+1} = -1 \end{cases} \\
&\quad \boldsymbol{b}^{\mathrm{L}} = \begin{bmatrix} b_1^{\mathrm{L}} & b_2^{\mathrm{L}} & \dots & b_e^{\mathrm{L}} & \dots & b_{E-1}^{\mathrm{L}} & b_E^{\mathrm{L}} \end{bmatrix} \\
&\qquad = \begin{bmatrix} x_1 & \overline{\theta_1} & \dots & \overline{\theta_{t-1}} & \dots & \overline{\theta_{T-1}} & \overline{\theta_T} \end{bmatrix} \\
&\quad \boldsymbol{b}^{\mathrm{U}} = \begin{bmatrix} b_1^{\mathrm{U}} & b_2^{\mathrm{U}} & \dots & b_e^{\mathrm{U}} & \dots & b_{E-1}^{\mathrm{U}} & b_E^{\mathrm{U}} \end{bmatrix} \\
&\qquad = \begin{bmatrix} \underline{\theta_1} & \underline{\theta_2} & \dots & \underline{\theta_t} & \dots & \underline{\theta_T} & x_H \end{bmatrix}
\end{aligned} \tag{S.16}$$

This relaxed problem is again pseudo-convex and can thus be solved to deterministic global optimality by means of interior-point algorithms. The obtained spline function parameters are referred to as $\boldsymbol{\beta}^{\mathrm{L}}$. The resulting objective function is a lower bound to the objective function:

$$\forall \boldsymbol{\theta} \in \Theta_l, \forall \boldsymbol{\beta} \in \Omega(\Theta_l, \boldsymbol{S}) : \underline{g} = \underline{g(\boldsymbol{\beta}^{\mathrm{L}})} \leq g(\boldsymbol{\beta}, \boldsymbol{\theta}) \tag{S.17}$$

Lower bound – Proof. Because the applied constraints in the modified lower bounding problem are always applied for any particular choice of $\boldsymbol{\theta}$ for the original problem, one can write that the feasible set for $\boldsymbol{\beta}$ in the lower bound case, $\Omega^{\mathrm{L}}(\underline{\boldsymbol{\theta}}, \overline{\boldsymbol{\theta}}, \boldsymbol{S})$, includes the feasible set for any feasible proposal for $\boldsymbol{\theta}$ for the original problem:

$$\forall \boldsymbol{\theta} \in \Theta_l : \Omega(\boldsymbol{\theta}, \boldsymbol{S}) \subseteq \Omega^{\mathrm{L}}(\underline{\boldsymbol{\theta}}, \overline{\boldsymbol{\theta}}, \boldsymbol{S}) \tag{S.18}$$

Given that the objective function and remaining constraints remain unchanged in the lower bound procedure, it holds that this procedure leads to a proven lower bound. This proves the validity of the lower bound.

S.2.2.4. Bounding gap. In a number of special cases, it can be shown that the lower bound solution will deliver the globally optimal solution within a considered set, Θ_l. This is only possible when the considered intervals defining Θ_l do not contain any spline basis knot inside their boundaries. Furthermore, this is only guaranteed when the transitions correspond only to changes in the signs of derivatives which are piece-wise linear or piece-wise quadratic in the function's argument. In the case of cubic spline functions, as used in this work, this corresponds to inflection points (2nd derivative is piece-wise linear) and extrema (1st derivative is piece-wise quadratic). This was demonstrated in Villez et al. (2013) for the univariate case ($J = 1, K = 1$). This property of the optimization problems means that the bounding gap during branch-and-bound optimization becomes zero in a finite number of steps, leading to absolute precision of the reported globally optimal solution. This property also holds for the extended SCS model studied in this work, however only when the number of considered spline functions is 1 ($J = 1$, without proof). No restrictions are required for the number of measured variables (K, without proof). In the general case ($J \geq 1$), an ϵ-optimal solution can be found in a finite number steps, with ϵ an arbitrary small strictly positive number.

S.2.2.5. Discontinuous trends. Locally discontinuous trends are not considered explicitly in this study, unlike Villez and Habermacher (2016). To allow the fitting of SCS functions with discontinuities one only needs to apply the additional relaxations of the optimization problem discussed in Villez and Habermacher (2016) to the multivariate case studied here. This leads again to a valid lower bound (without proof). The upper bound provided in this work remains valid in its current form (without proof). Even though such adjustments are not studied in detail in this work, they are implemented within the provided software toolbox for SCS function fitting.

S.3. Additional figures

S.3.1. Setup

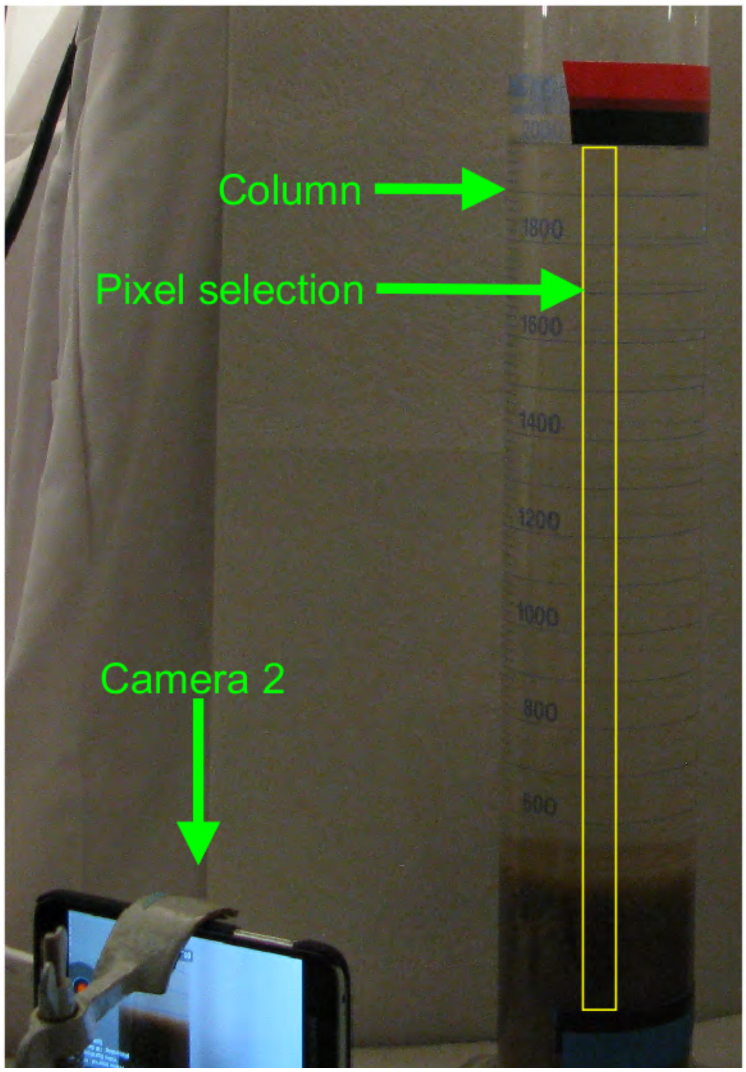

Figure S.1: Experiment 6 - Image 42. This image is registered with camera 1. The yellow rectangle indicate the selected area for analysis. Camera 2 is visible at the bottom of the image left of the column.

S.3.2. Experiment 1

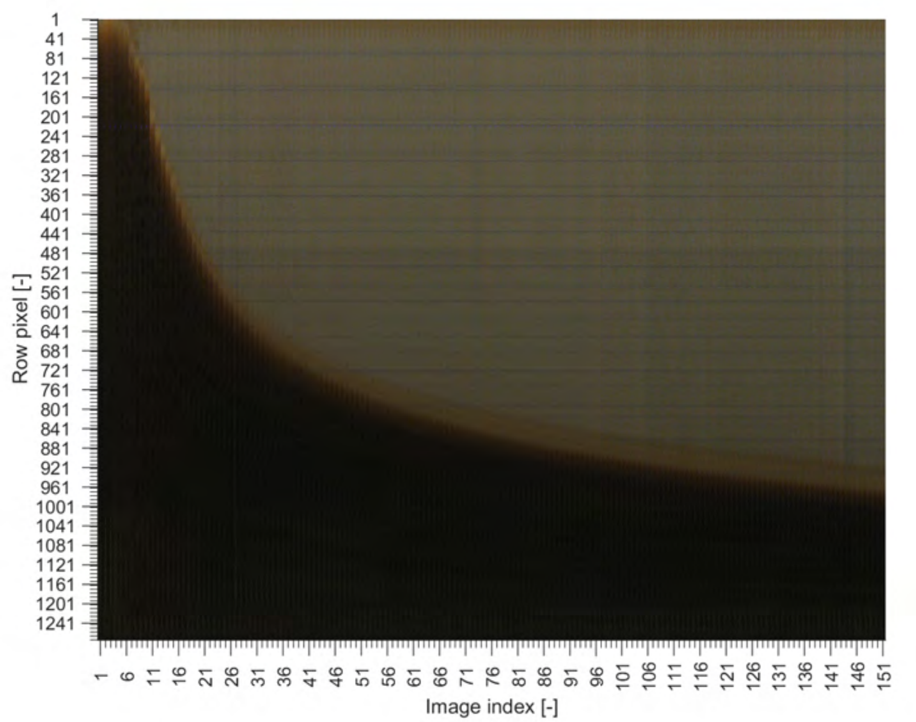

Figure S.2: Experiment 1 – Composite image.

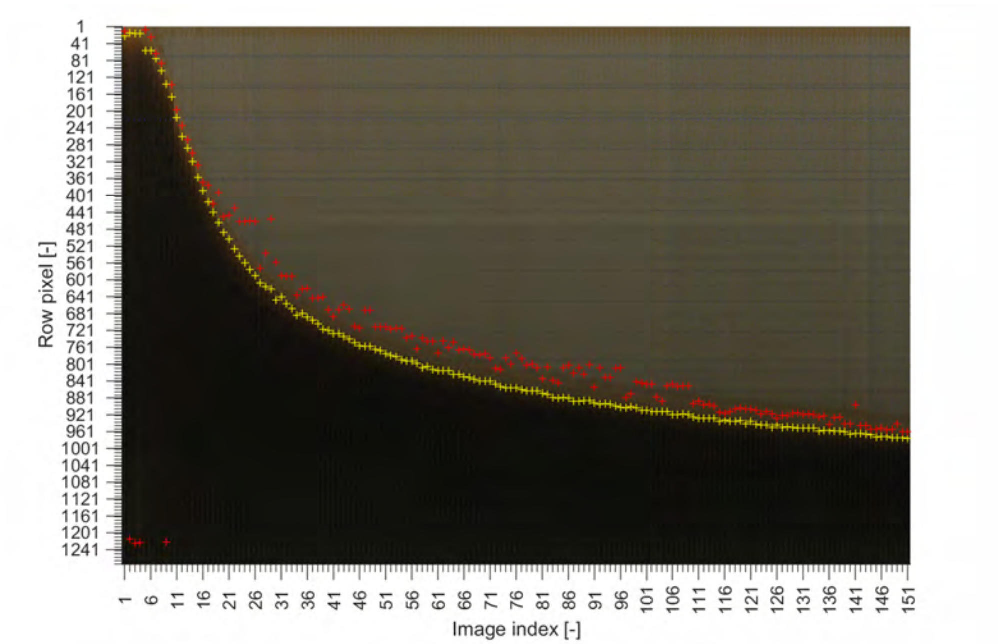

Figure S.3: Experiment 1 – Composite image with indications of the sludge blanket height identified via shape constrained spline fitting.

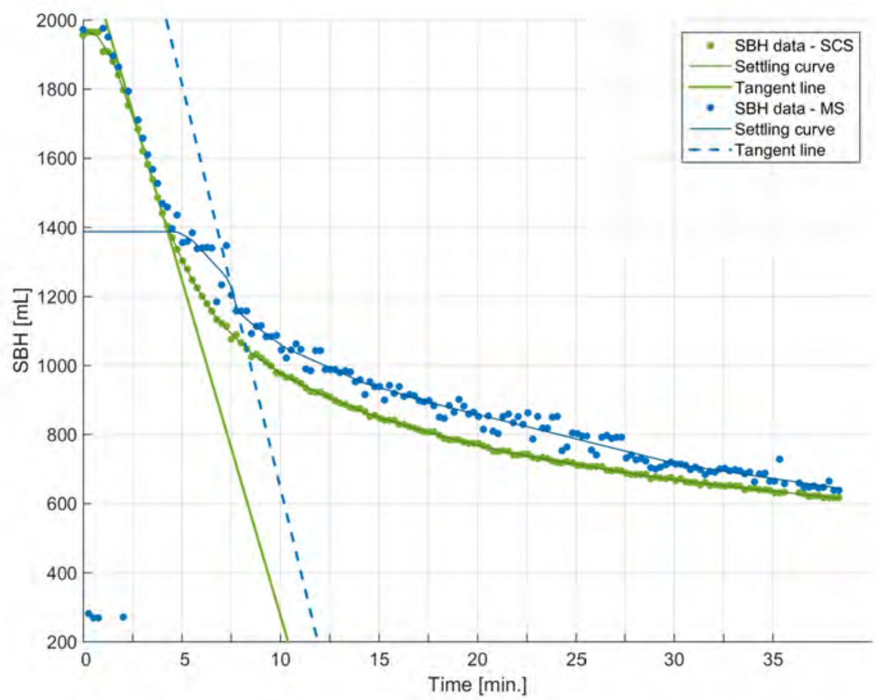

Figure S.4: Experiment 1 – Batch settling curve, inflection point, and tangent line obtained with the SCS and MS method for SBH registration.

S.3.3. Experiment 2

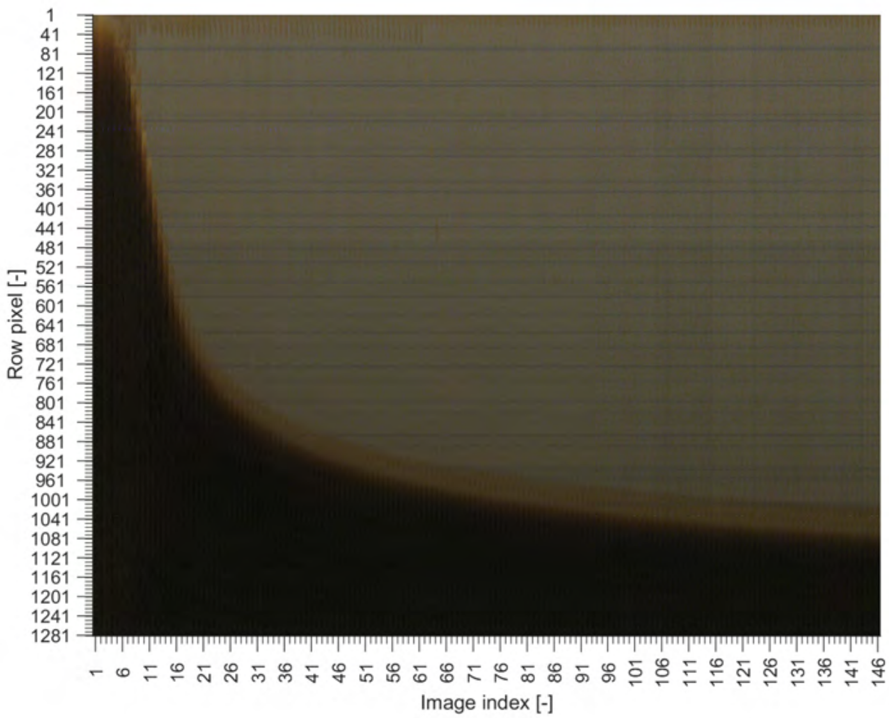

Figure S.5: Experiment 2 – Composite image.

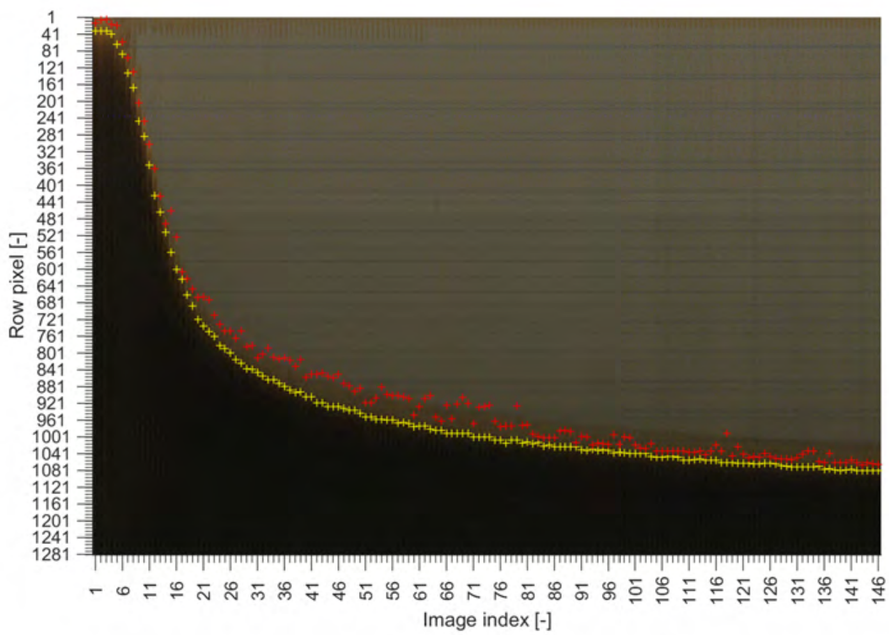

Figure S.6: Experiment 2 – Composite image with indications of the sludge blanket height identified via shape constrained spline fitting.

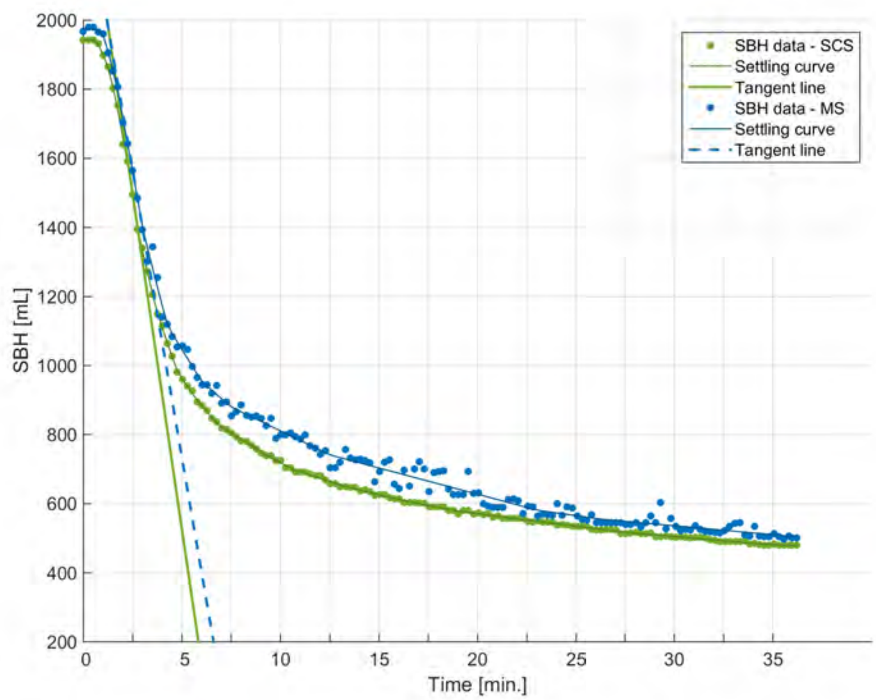

Figure S.7: Experiment 2 – Batch settling curve, inflection point, and tangent line obtained with the SCS and MS method for SBH registration.

S.3.4. Experiment 3

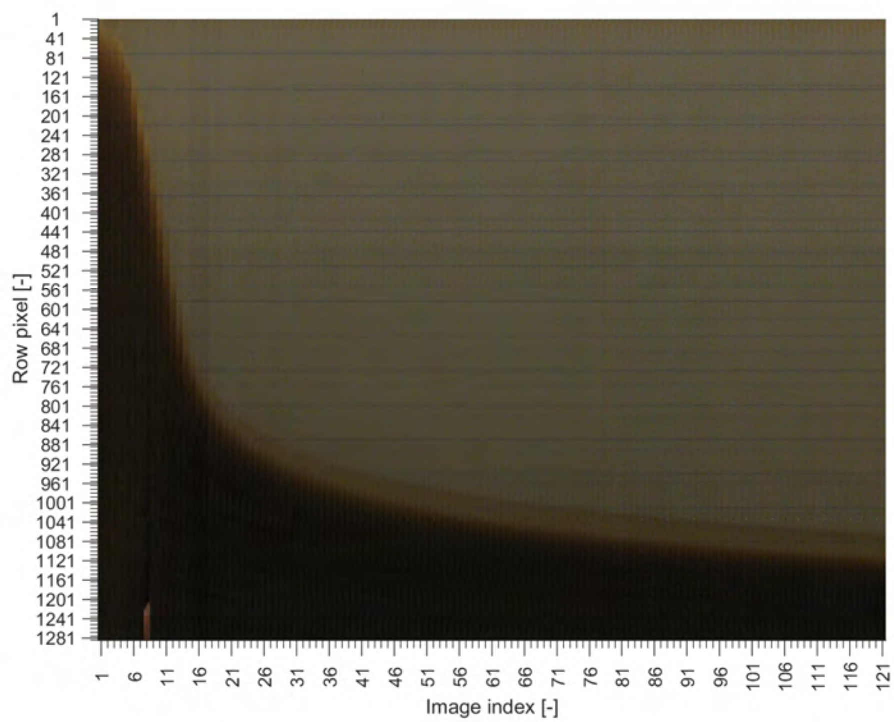

Figure S.8: Experiment 3 – Composite image.

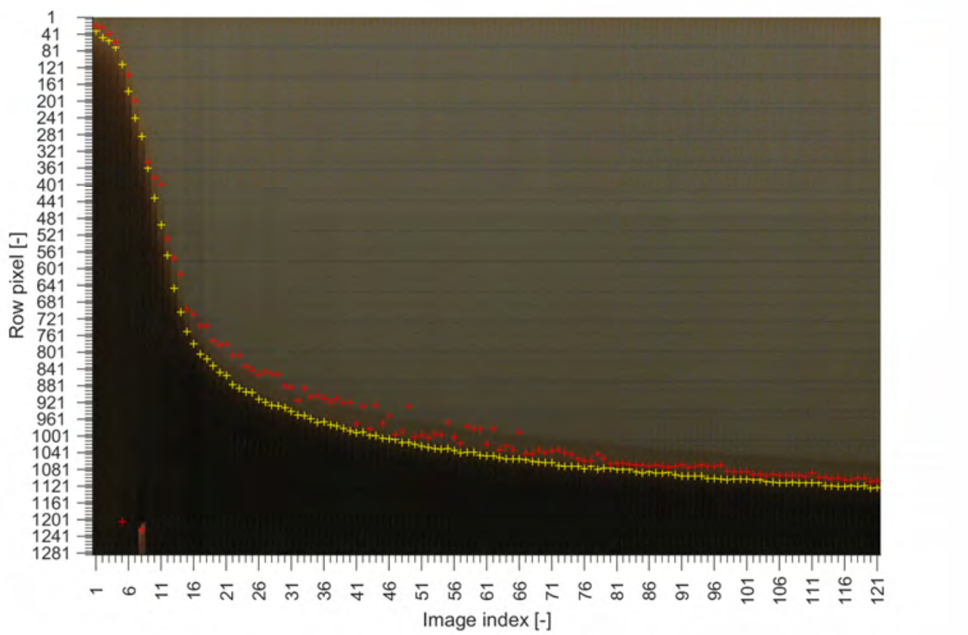

Figure S.9: Experiment 3 – Composite image with indications of the sludge blanket height identified via the SCS (yellow) and MS (red) method.

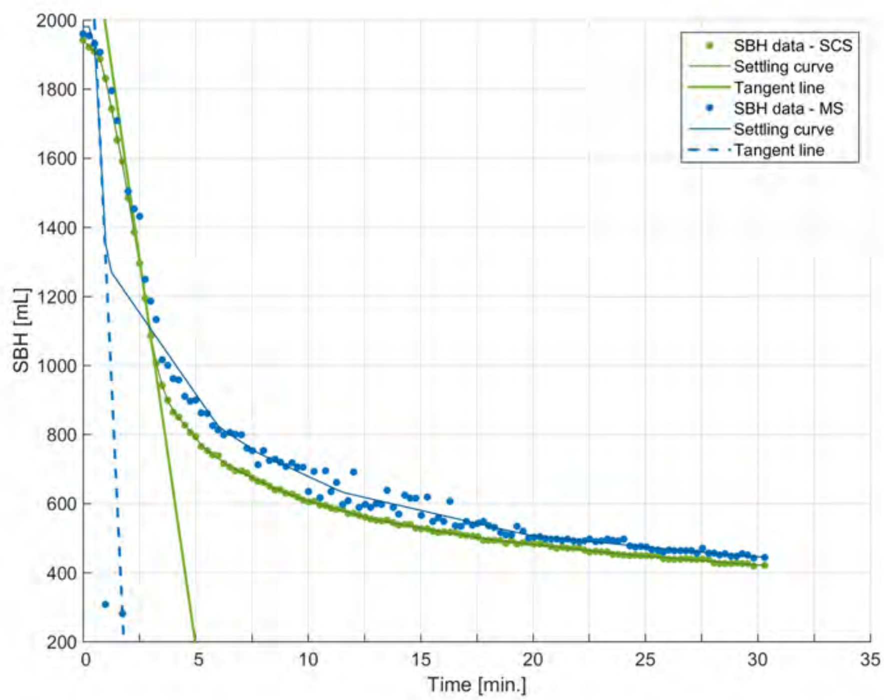

Figure S.10: Experiment 3 – Batch settling curve, inflection point, and tangent line obtained with the SCS and MS method for SBH registration.

S.3.5. Experiment 4

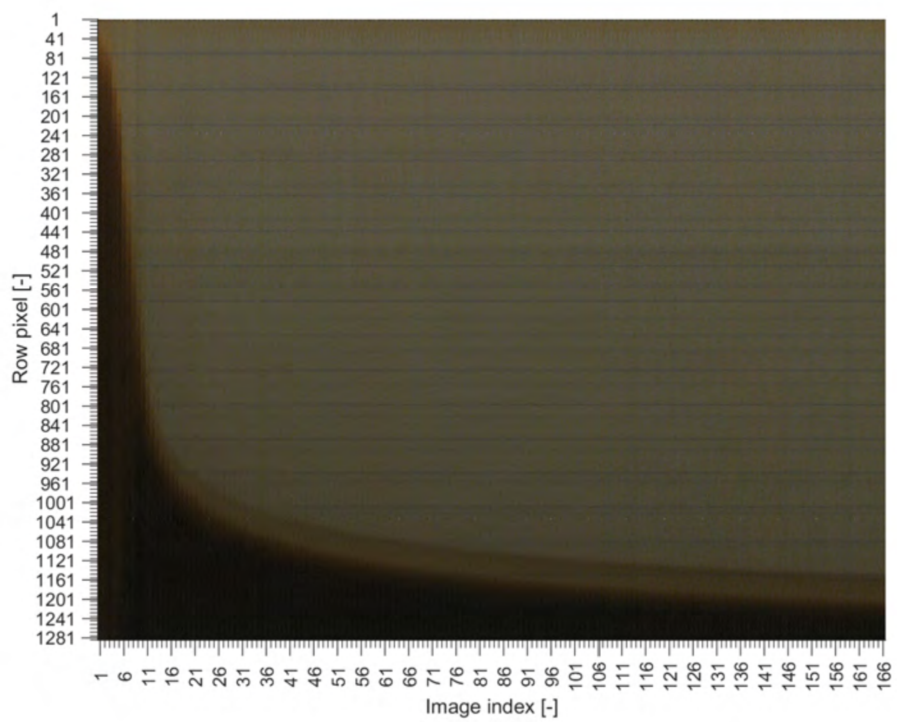

Figure S.11: Experiment 4 – Composite image.

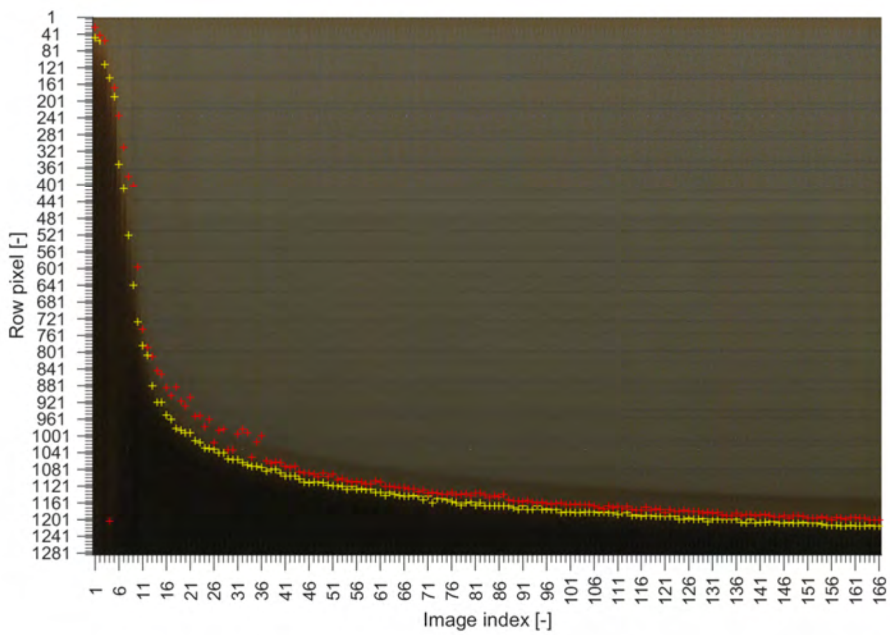

Figure S.12: Experiment 4 – Composite image with indications of the sludge blanket height identified via the SCS (yellow) and MS (red) method.

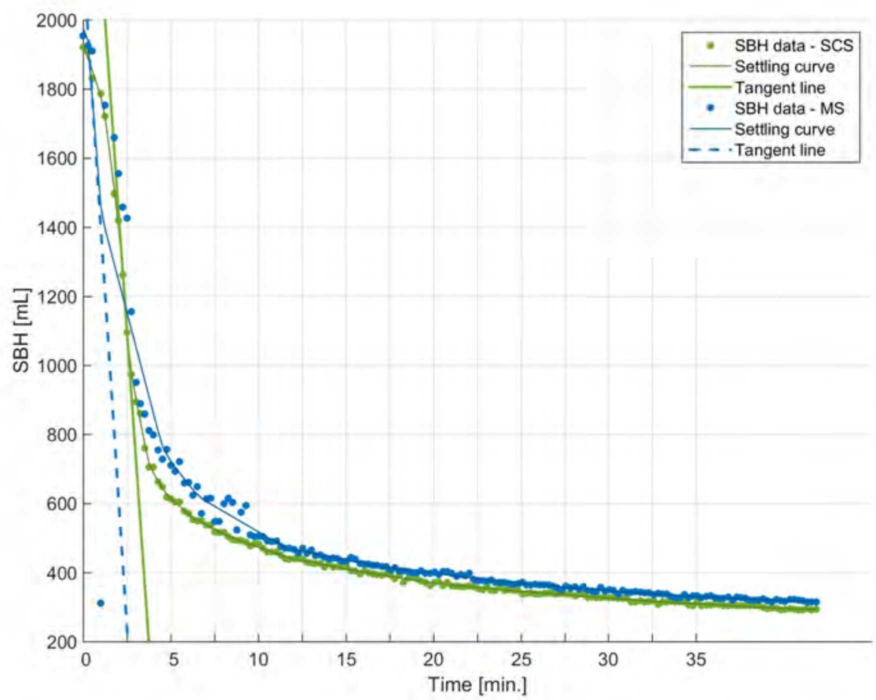

Figure S.13: Experiment 4 – Batch settling curve, inflection point, and tangent line obtained with the SCS and MS method for SBH registration.

S.3.6. Experiment 5

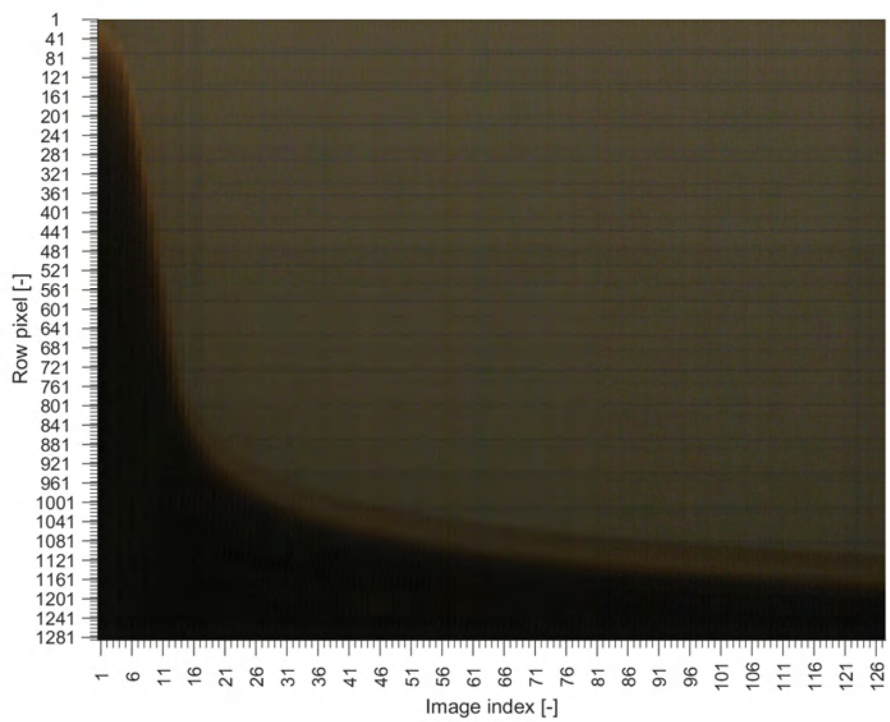

Figure S.14: Experiment 5 – Composite image.

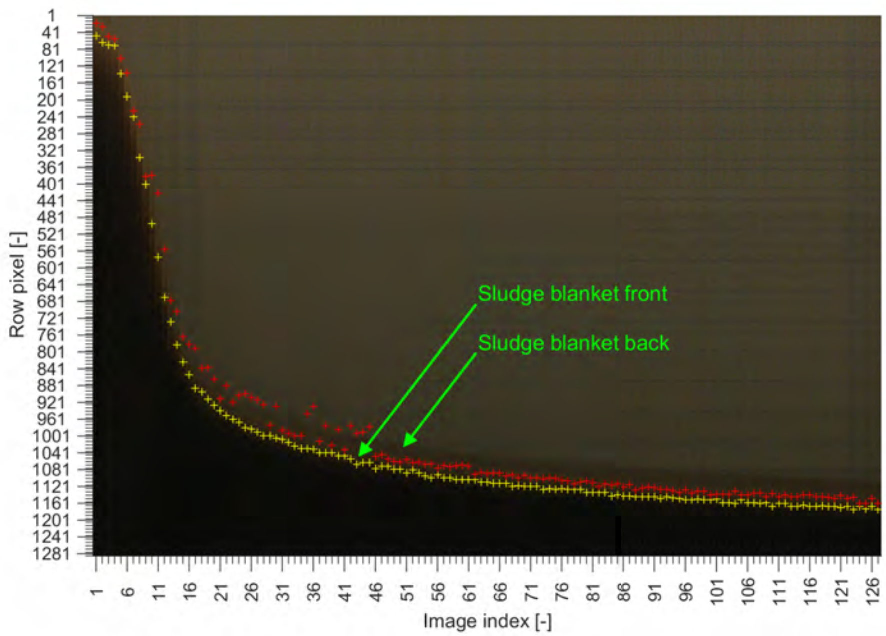

Figure S.15: Experiment 5 – Composite image with indications of the sludge blanket height identified via the SCS (yellow) and MS (red) method.

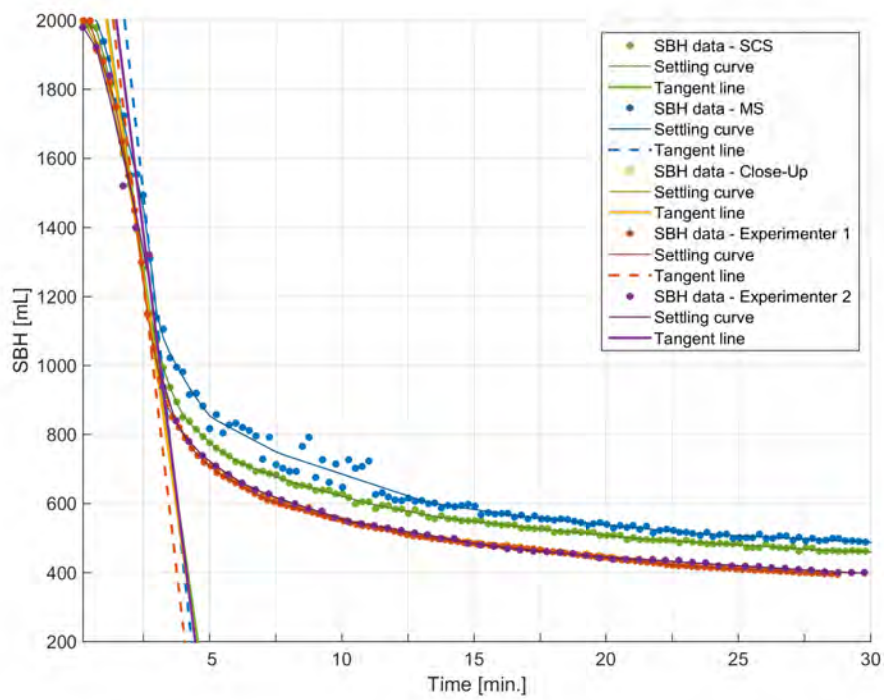

Figure S.16: Experiment 5 – Batch settling curves, inflection points, and tangent lines obtained with all SBH profiles.

S.3.7. Experiment 6

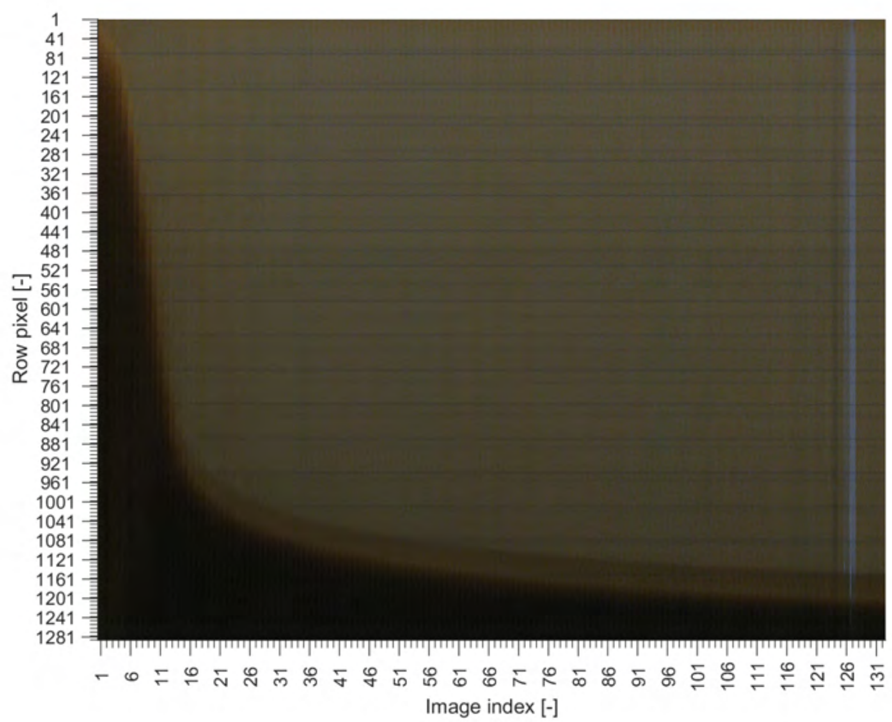

Figure S.17: Experiment 6 – Composite image.

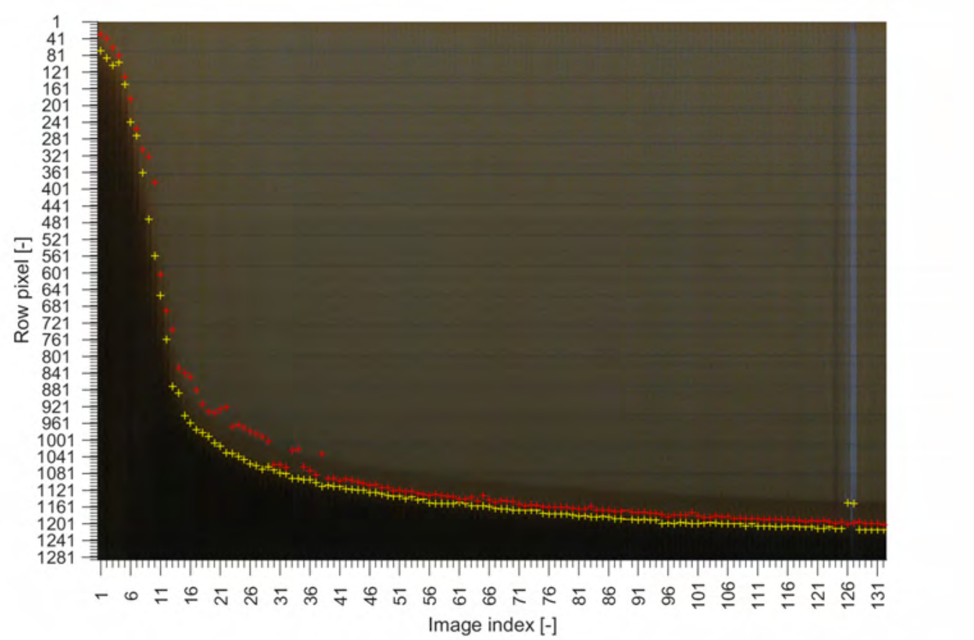

Figure S.18: Experiment 6 – Composite image with indications of the sludge blanket height identified via the SCS (yellow) and MS (red) method.

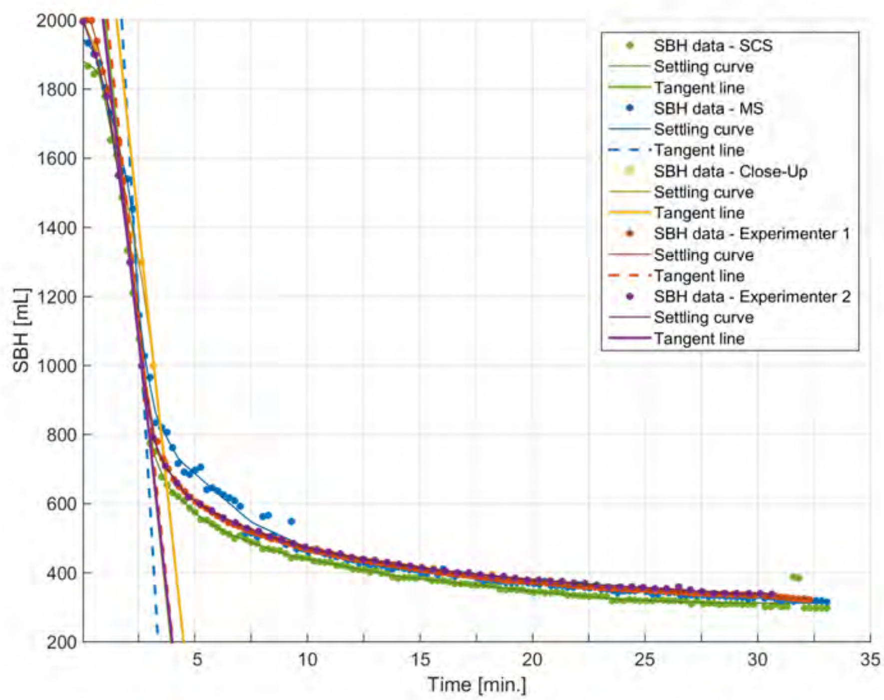

Figure S.19: Experiment 6 – Batch settling curves, inflection points, and tangent lines obtained with all SBH profiles.

S.3.8. Experiment 7

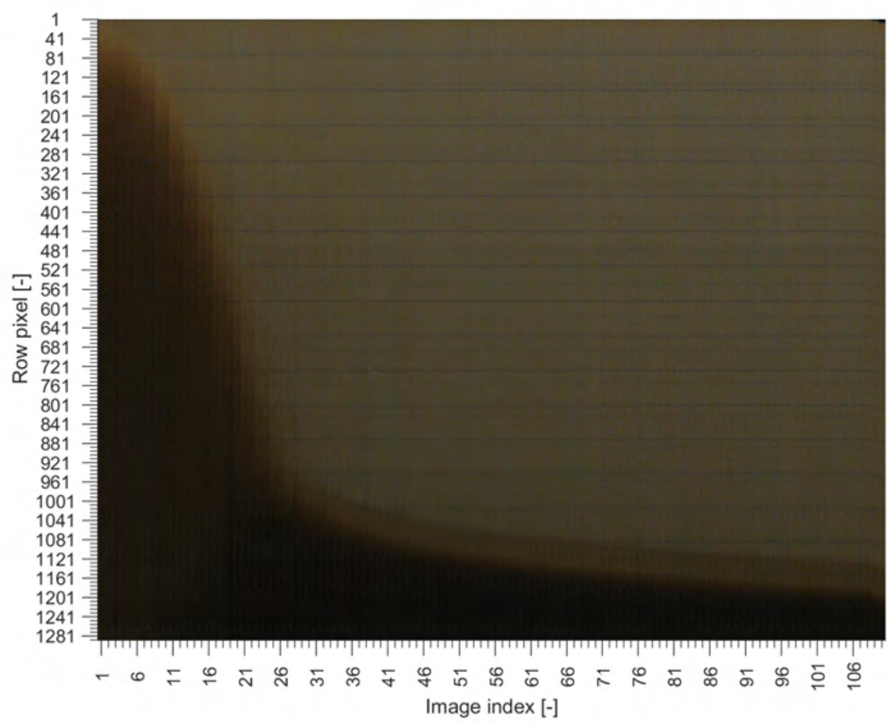

Figure S.20: Experiment 7 – Composite image.

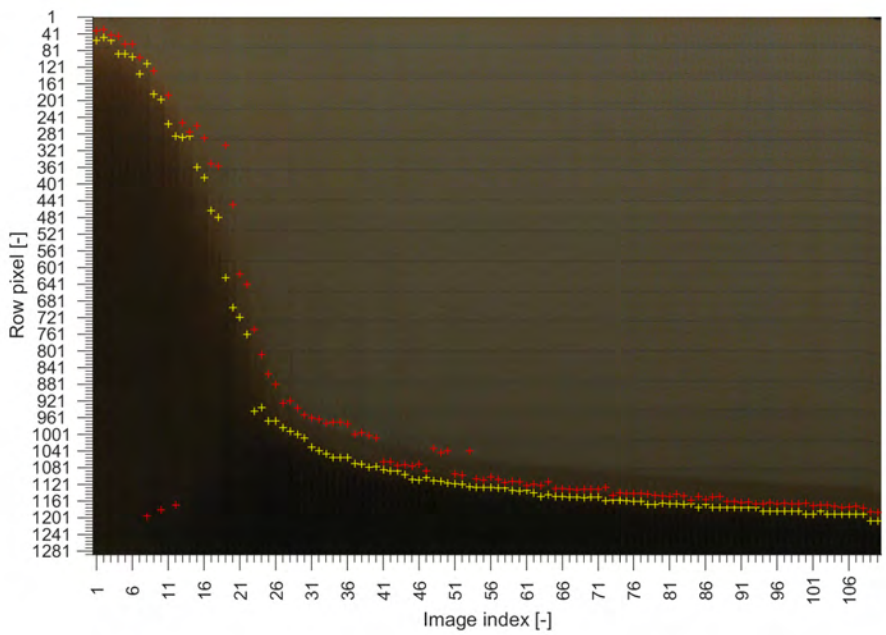

Figure S.21: Experiment 7 – Composite image with indications of the sludge blanket height identified via the SCS (yellow) and MS (red) method.

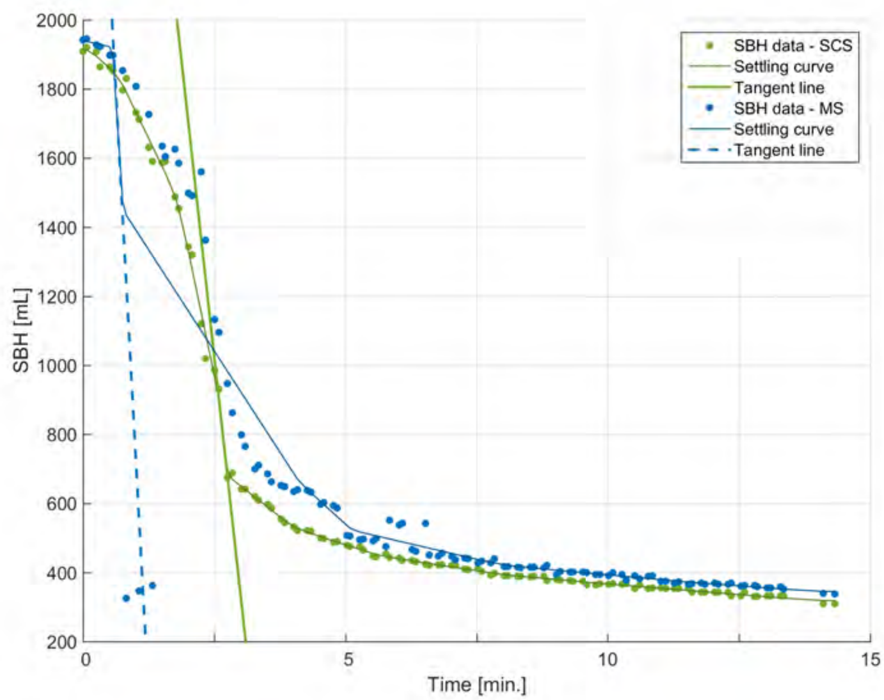

Figure S.22: Experiment 7 – Batch settling curve, inflection point, and tangent line obtained with the SCS and MS method for SBH registration.

S.3.9. Experiment 8

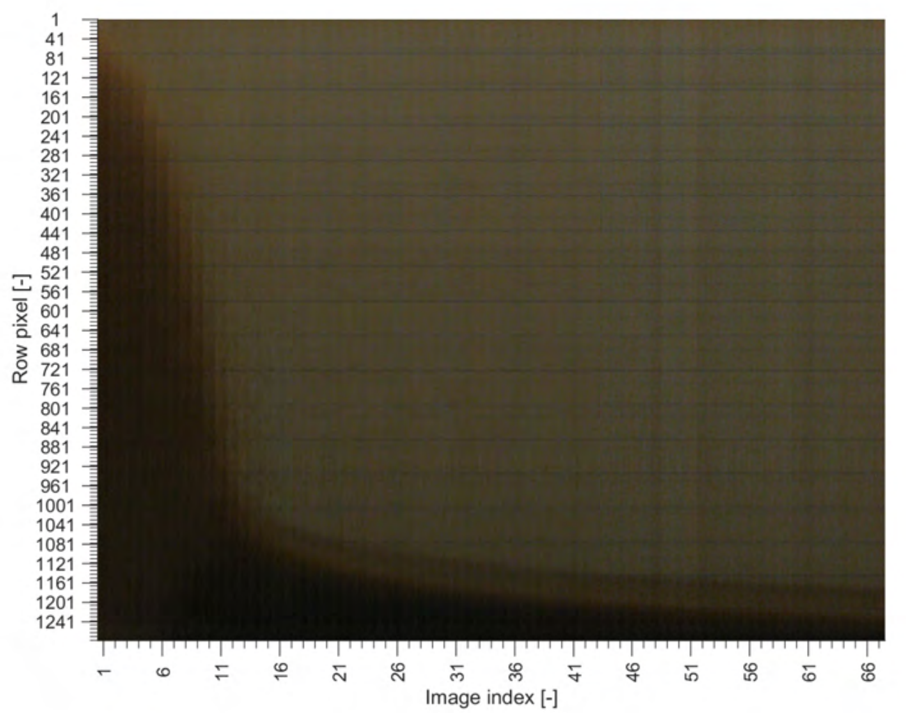

Figure S.23: Experiment 8 – Composite image.

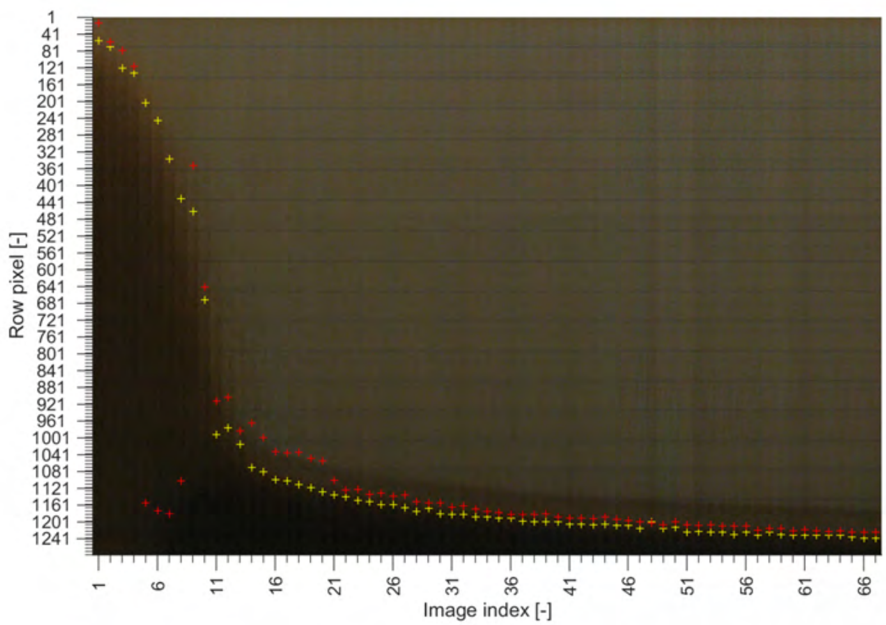

Figure S.24: Experiment 8 – Composite image with indications of the sludge blanket height identified via the SCS (yellow) and MS (red) method.

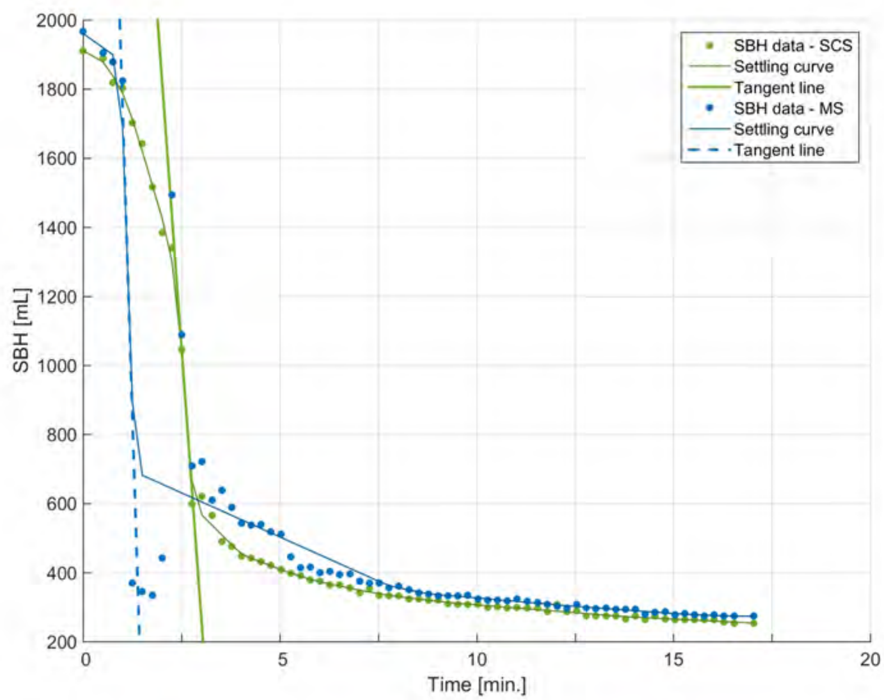

Figure S.25: Experiment 8 – Batch settling curve, inflection point, and tangent line obtained with the SCS and MS method for SBH registration.

S.3.10. Experiment 9

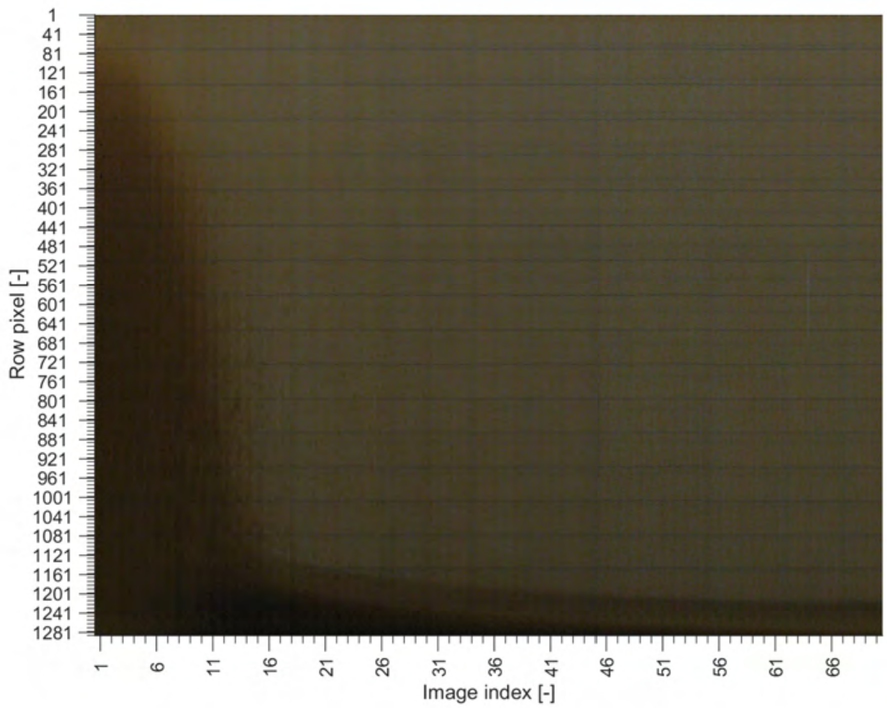

Figure S.26: Experiment 9 – Composite image.

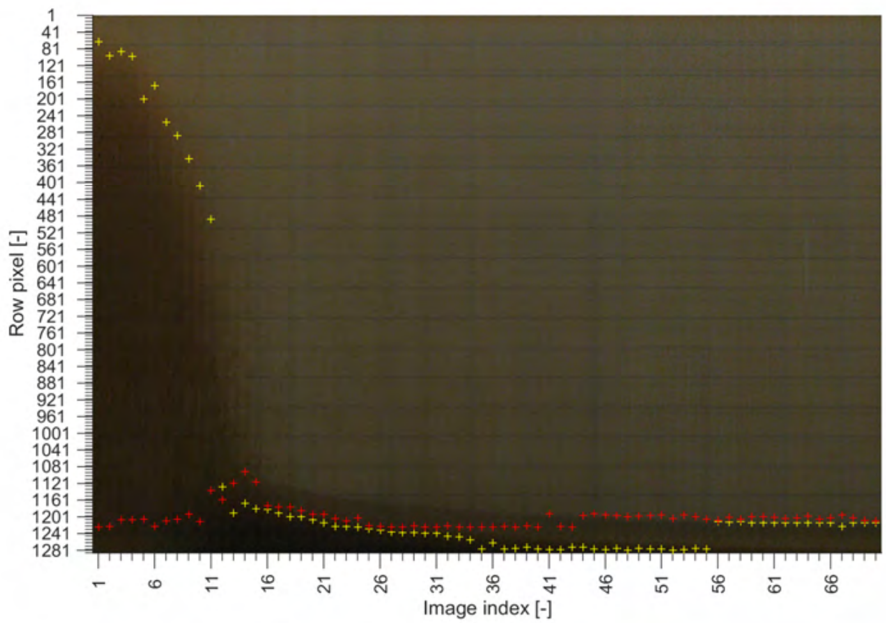

Figure S.27: Experiment 9 – Composite image with indications of the sludge blanket height identified via the SCS (yellow) and MS (red) method.

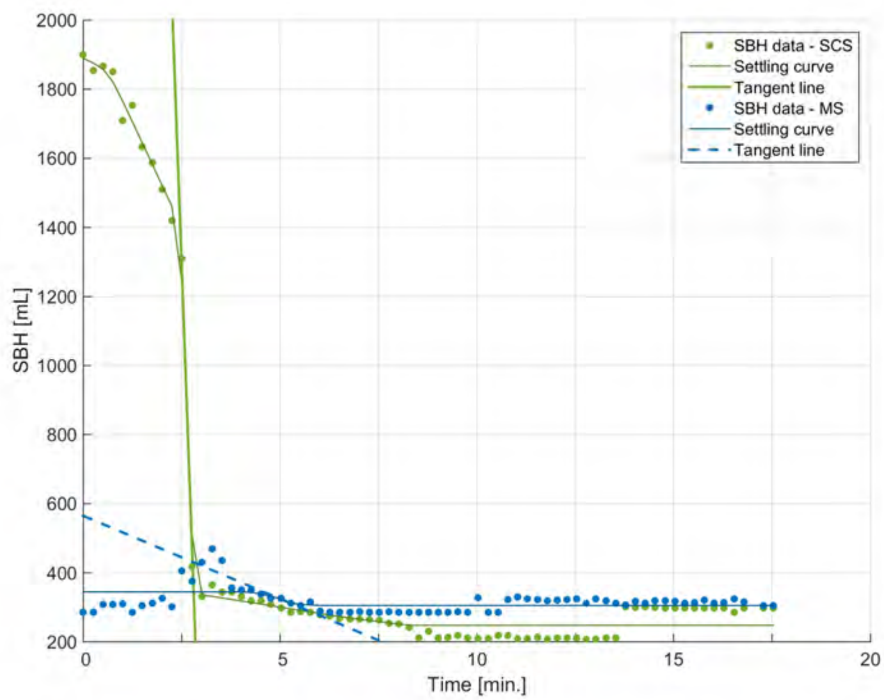

Figure S.28: Experiment 9 – Batch settling curve, inflection point, and tangent line obtained with the SCS and MS method for SBH registration.